UNIVERSITY OF HELSINKI REPORT SERIES IN PHYSICS

HU-P-D188

Modelling vacuum arcs:
from plasma initiation to surface interactions

Helga Timkó

Division of Materials Physics
Department of Physics
Faculty of Science
University of Helsinki
Helsinki, Finland

ACADEMIC DISSERTATION

To be presented, with the permission of the Faculty of Science of the University of Helsinki, for public criticism in the Auditorium XV of the University Main building (Fabianinkatu 33), on 10th December 2011, at 10 o'clock.

HELSINKI 2011

ISBN 978-952-10-7074-7 (printed version)
ISSN 0356-0961
Helsinki 2011
Helsinki University Printing House (Yliopistopaino)

ISBN 978-952-10-7075-4 (PDF version)
http://ethesis.helsinki.fi/
Helsinki 2011
Electronic Publications @ University of Helsinki (Helsingin yliopiston verkkojulkaisut)

Helga Timkó **Modelling vacuum arcs: from plasma initiation to surface interactions**, University of Helsinki, 2011, 60 p.+appendices, University of Helsinki Report Series in Physics, HU-P-D188, ISSN 0356-0961, ISBN 978-952-10-7074-7 (printed version), ISBN 978-952-10-7075-4 (PDF version)

Classification (INSPEC): A5280M, A5280V, A5240H, A5265, A6185, A2915D
Keywords (INSPEC): arcs and sparks, discharges in vacuum, solid-plasma interactions, plasma simulation, molecular dynamics simulation, linear accelerators

Abstract

A better understanding of vacuum arcs is desirable in many of today's 'big science' projects including linear colliders, fusion devices, and satellite systems. For the Compact Linear Collider (CLIC) design, radio-frequency (RF) breakdowns occurring in accelerating cavities influence efficiency optimisation and cost reduction issues. Studying vacuum arcs both theoretically as well as experimentally under well-defined and reproducible direct-current (DC) conditions is the first step towards exploring RF breakdowns.

In this thesis, we have studied Cu DC vacuum arcs with a combination of experiments, a particle-in-cell (PIC) model of the arc plasma, and molecular dynamics (MD) simulations of the subsequent surface damaging mechanism. We have also developed the 2D ARC-PIC code and the physics model incorporated in it, especially for the purpose of modelling the plasma initiation in vacuum arcs.

Assuming the presence of a field emitter at the cathode initially, we have identified the conditions for plasma formation and have studied the transitions from field emission stage to a fully developed arc. The 'footing' of the plasma is the cathode spot that supplies the arc continuously with particles; the high-density core of the plasma is located above this cathode spot. Our results have shown that once an arc plasma is initiated, and as long as energy is available, the arc is self-maintaining due to the plasma sheath that ensures enhanced field emission and sputtering.

The plasma model can already give an estimate on how the time-to-breakdown changes with the neutral evaporation rate, which is yet to be determined by atomistic simulations. Due to the non-linearity of the problem, we have also performed a code-to-code comparison. The reproducibility of plasma behaviour and time-to-breakdown with independent codes increased confidence in the results presented here.

Our MD simulations identified high-flux, high-energy ion bombardment as a possible mechanism forming the early-stage surface damage in vacuum arcs. In this mechanism, sputtering occurs mostly in clusters, as a consequence of overlapping heat spikes. Different-sized experimental and simulated craters were found to be self-similar with a crater depth-to-width ratio of about 0.23 (sim) – 0.26 (exp).

Experiments, which we carried out to investigate the energy dependence of DC breakdown properties, point at an intrinsic connection between DC and RF scaling laws and suggest the possibility of accumulative effects influencing the field enhancement factor.

Contents

List of constants and variables

Unless stated otherwise, SI-units are used in this thesis.

Constant	Value	Quantity
e	$1.602\,176\,487 \times 10^{-19}$ C	elementary charge
$\hbar$	$1.054\,571\,628 \times 10^{-34}$ J s	reduced Planck constant
ε_0	$8.854\,187\,817 \times 10^{-12}$ F/m	permittivity of free space

Variable	Quantity
$\mathbf{a}_\mathrm{p}$	acceleration of particle p
$\mathbf{B}$	magnetic field
$\mathbf{E}$	electric field
E_b	breakdown field
E_loc	local field
E_sat	saturated field
f	distribution function
$\mathbf{F}_\mathrm{p}$	force acting on particle p
j_melt	threshold of field emission current density that melts the emitter
j_FN	electron field emission current density
m_p	mass of particle p
n_p	number density of species p
p	pressure
r	radial distance in the cylindrical coordinate system
$r_\mathrm{Cu/e}$	neutral evaporation to electron field emission ratio
R_em	emission radius of the field emitter
R_inj	injection radius of field emission electrons and evaporated neutrals
$\mathbf{r}_\mathrm{p}$	coordinate of particle p
T	temperature (in units of energy)
$\mathbf{v}_\mathrm{p}$	velocity of particle p
v_rel	relative velocity of two particles
z	height coordinate in the cylindrical coordinate system
β	field enhancement factor
β_f	field enhancement factor of the flat surface
Γ	ionisation rate
Δt	time step
Δz, Δr	grid size

Variable	Quantity
ϑ	azimuth in the cylindrical coordinate system
λ_{Db}	Debye length
$\ln(\lambda)$	Coulomb logarithm
σ	collision cross-section
ϕ	work function
φ	electric potential
ω_{pe}	plasma frequency

1 Introduction

Vacuum discharges may appear in different forms in almost every area of today's big science projects — may it be unipolar arcs in fusion devices [1–5], multipactor discharges in satellite systems [6–8], or vacuum arcs in future accelerator designs [9, 10]. Often these discharges are undesired; however, they may also be used in industry in a controlled manner like in electrical discharge machining [11, 12], arc welding [13, 14], cutting [15], or in ignition devices [16, 17]. Gaseous arcs and electrical discharges such as lightnings have been known since ancient times and the processes ongoing in a discharge lamp, for instance, are relatively well understood by now [18, 19]. In contrast, surprisingly little is understood about the underlying mechanisms of the formation and evolution of vacuum arcs [20, 21] that can 'mystically' form even in ultra high vacuum (UHV) conditions, where practically no medium between the electrodes is present.

The Compact Linear Collider (CLIC) Study aims at developing a realistic technology for a future normal-conducting electron-positron linear collider in the multi-TeV centre of mass energy range [22]. At the limit of the conventional accelerating technique, the 'compactness' of the machine calls for a high accelerating gradient of 100 MV/m [23], while its efficiency relies on a low breakdown probability of a few 10^{-7} 1/pulse/m [24], since every vacuum arc in the machine causes a bunch loss. The constraint on breakdown probability is governed by (i) accelerating length, (ii) pulse repetition rate, and (iii) the efficiency to be achieved at the interaction point. Reducing the breakdown probability, however, is desirable not only from the luminosity point of view. Given the high estimated power consumption of the proposed design (415 MW [25]), efficiency optimisation through breakdown probability reduction could lead to a significant reduction in operation costs as well.

The present 12 GHz radio-frequency (RF) CLIC accelerating cavity testing strives for performance optimisation in order to lay down a baseline concept for the accelerating cavities. When testing these cavities, incident, transmitted, and reflected signals are monitored all the time. While normally the transmitted signal is almost the same as the incident signal, on some pulses the transmission drops suddenly to roughly zero and the reflection becomes significant, indicating a breakdown has occurred.

Although RF cavity tests are the most direct way to explore vacuum arcs in CLIC, cavity testing is time-consuming and costly; thus these tests are not well-suited for studying vacuum arcs. Instead, vacuum arcs can be generated cost-efficiently and in a controlled manner in two direct-current (DC) setups at CERN [26, 27]. Despite intrinsic differences between DC and RF testing, the measurement environment (electric field, pressure in the vacuum chamber, energy available for

breakdown) in the DC setups is matched to RF cavity parameters as closely as possible.

Since it is generally believed that we need to understand DC vacuum arcs, before we can generalise to RF, a theoretical model is also expected to be first directed at DC vacuum arcs. A full model of vacuum arcs would have to be able to treat many different processes occurring at different stages. Amongst others, it should be able to explain (i) what surface features may trigger the field emission of electrons in the first place [28–31], (ii) how these features may serve as a source of non-electron species [32, 33], that is, why breakdowns under vacuum can occur at all, (iii) how these features can be created in the presence of a high electric field [34, 35], (iv) how a plasma forms and evolves subsequently, and finally, (v) how vacuum arcs damage the cathode surface. The main focus of this thesis will be on the latter two points.

Over the past fifty or sixty years, much time and effort has been invested into the observation of different properties of vacuum arcs and, as a consequence, a vast amount of experimentally acquired knowledge has been accumulated. In order to understand the complex correlation between different observations and moreover, in order to make predictions, a theoretical approach to the problem is needed as well. However, despite an equally vast amount of theoretical attempts to explain and predict certain vacuum arc properties, a model that can describe vacuum arcs in their entirety and complexity has not been successfully developed yet. Thus both industry and today's big science projects keenly await the development of such a model of vacuum arcs.

2 Purpose and structure of this study

2.1 Motivation

The purpose of this study is to better understand the complex plasma-wall interactions that occur in a vacuum arc. When modelling a transient, non-linear problem, a constant and mutual interplay between theory and experiments turns out to be an indispensable tool, just as code-to-code comparisons are. One of the plasma-wall interactions that has been investigated is the cathode surface damage caused by the vacuum arc plasma, which provides perhaps the most direct link to experimental observations. A more specific purpose of this study was to obtain a qualitative picture of the plasma initiation phase after having developed the appropriate tools to this end: a physics model and a computer code.

The thesis consists of a thesis summary and seven publications, referred to with Roman bold numbers, six of which have been either published in, accepted in, or submitted to international peer-reviewed journals and one has been published as a CERN internal technical note.

This thesis is organised as follows: in this Section, a short description of each publication and the author's contribution is given. Vacuum arcs are described in Sec. 3. Details on experimental and numerical methods, as well as on the physics model are given in Sec. 4. All experimental and modelling results are presented in Sec. 5. Conclusions are drawn in Sec. 6. After the acknowledgements and list of references, the below mentioned publications are attached.

2.2 Summaries of the original publications

In publication **I**, experimental results of the energy dependence measurements of processing and breakdown properties, obtained with the DC setup, are detailed. A one- and a two-dimensional particle-in-cell (PIC) model of plasma initiation in vacuum arcs is presented in publications **II** and **III**, respectively. The software developed for the two-dimensional model is described in **IV**. A code-to-code benchmarking study with a simplified discharge model is presented in **V**. The mechanism of cathode crater formation due to plasma ions is investigated with the molecular dynamics (MD) method in **VI** and is compared to the damage caused by cluster ion bombardment in **VII**.

Publication I:
Energy Dependence of Processing and Breakdown Properties of Cu and Mo,
H. Timko, M. Aicheler, P. Alknes, S. Calatroni, A. Oltedal, A. Toerklep, M. Taborelli, W. Wuensch, F. Djurabekova, and K. Nordlund, *Physical Review Special Topics – Accelerators and Beams* **14**, 101003 (2011).

Experimental results on the energy dependence of Cu and Mo properties measured under DC conditions are presented in this publication. Besides studying the dependence of the field enhancement factor, saturated field, local field, and damaged area of Cu and Mo on the energy available for breakdown, a relation between processing efficiency and energy is established as well. For Mo, a possible explanation of the DC processing mechanism is concluded. The measurements also imply that certain scaling laws derived from RF cavity testing are valid in DC as well.

Publication II:

A One-Dimensional Particle-in-Cell Model of Plasma Build-Up in Vacuum Arcs,

H. Timko, K. Matyash, R. Schneider, F. Djurabekova, K. Nordlund, A. Hansen, A. Descoeudres, J. Kovermann, A. Grudiev, W. Wuensch, S. Calatroni, and M. Taborelli, *Contributions to Plasma Physics* **51**, 5–21 (2011).

The publication presents a newly developed physics model embedded in a one-dimensional PIC code, which describes plasma initiation based on the assumption that a field-enhancing feature is initially present on the cathode. The model includes field emission and neutral evaporation as initiator mechanisms, and takes several surface processes and collisions into account. Extensive simulations show how different factors in the model affect, amongst other things, both the time-to-breakdown and properties of the field emitter. Furthermore, they also identify the prerequisites for a breakdown to occur.

Publication III:

Modeling of cathode plasma initiation in copper vacuum arc discharges via particle-in-cell simulations,

H. Timko, K. Matyash, R. Schneider, F. Djurabekova, K. Nordlund, S. Calatroni, and W. Wuensch, *Physics of Plasmas*, submitted for publication (2011).

The previous model has been refined and adapted to a two-dimensional PIC model. This study focuses on the temporal and spatial evolution of vacuum arcs in their plasma initiation phase and their interpretation with respect to experimental findings. It identifies the different transitions leading from field emission to a self-maintaining arc and demonstrates how an arc spot can spread and potentially initiate other spots at the cathode. With a realistic modelling of the boundary conditions of the potential, the current-voltage characteristic of arcs is qualitatively investigated, and thus the model addresses how a steady-state, low-burning-voltage arc is established.

Publication IV:

2D Arc-PIC Code Description: Methods and Documentation,

H. Timko, *Technical Report, CERN, CLIC Note* **872**, (2011).

The two-dimensional PIC code developed specifically for the purpose of the above and future studies is described in detail in this technical note. In the first part, the different methods used in the code for the field solver, particle pusher, charge assignment and field interpolation schemes, collisions, etc. are described. Particular features related to the modelling of vacuum arcs are specified as well. The second part contains a comprehensive list of equations used in the code, including their derivation and re-scaling (for efficiency, all equations in the code are dimensionless).

PUBLICATION V:

Why perform code-to-code comparisons: a vacuum arc discharge simulation case study,
H. Timko, P. S. Crozier, M. M. Hopkins, K. Matyash, and R. Schneider, *Contributions to Plasma Physics*, accepted for publication (2011).

This publication reports on the outcome of a code-to-code comparison between the 1D ARC-PIC and the two-dimensional ALEPH codes, carried out with a simplified vacuum arc model. After identifying and remedying some software flaws in ALEPH, an excellent agreement in time-to-breakdown and current density predictions is achieved. Moreover, this benchmarking 'exercise' has shown how a given choice of different numerical methods can influence the results when a non-linear, transient problem is modelled.

PUBLICATION VI:

Mechanism of surface modification in the plasma-surface interaction in electrical arcs,
H. Timko, F. Djurabekova, K. Nordlund, L. Costelle, K. Matyash, R. Schneider, A. Toerklep, G. Arnau-Izquierdo, A. Descoeudres, S. Calatroni, M. Taborelli, and W. Wuensch, *Physical Review B* **81**, 184109 (2010).

Knowing the properties of plasma ions impinging on the cathode surface, the resulting surface damage and crater formation was investigated with the MD method. Complex crater shapes as seen in experiments can form as a result of a heat spike sputtering process, which is due to the high flux and energy of impinging particles. This heat spike sputtering also leads to an enhanced sputtering yield in the presence of the plasma. Sputtering takes place mainly in clusters, explaining finger-like structures observed experimentally. Both simulated and measured crater profiles are shown to be self-similar over several orders of magnitude, with a characteristic depth-to-width ratio.

PUBLICATION VII:

Crater formation by single ions, cluster ions and ion "showers",
F. Djurabekova, J. Samela, H. Timko, K. Nordlund, S. Calatroni, M. Taborelli, and W. Wuensch,

Nuclear Instruments and Methods in Physics Research B, article in press (2011).

The connection between crater formation mechanisms due to (i) high-flux single ion impact (ion 'showers') and due to (ii) densely packed cluster ions was investigated for 500 eV Au ions. In both cases, a similar damage can be observed. However, the underlying crater formation mechanism differs: while 'showers' create damage through overlapping heat spikes, cluster ions lead to explosive cratering that can be identified through an over-densified front on the surface after the impact.

2.3 AUTHOR'S CONTRIBUTION

A substantial part of the experiments presented in publication **I** was carried out and the rest was supervised by the author of this thesis, who also suggested and planned the measurements of spot size development and processing. The data analysis and publication writing was all completed by the author.

The vacuum arc physics model in **II** was developed and implemented in the 1D ARC-PIC code by the author. The author also carried out all simulations and data analysis, and wrote the publication.

The 2D ARC-PIC code and the refined physics model described in **III** was developed by the author, who also performed the simulations and data analysis, and wrote the publication.

The author wrote the entire 2D ARC-PIC code documentation presented in **IV** and derived the re-scaled equations therein.

All simulations carried out with the 1D ARC-PIC code in **V** were performed by the author. The author also did all the data analysis, and wrote most of the text of the publication, apart from the ALEPH code description and part of the introduction.

After some initial simulations by co-authors, all systematic simulations and data analysis in **VI** was carried out by the author, who also took part in the measurements and wrote most of the Methods section.

In **VII**, the author performed the Cu simulations mentioned in the text and provided consultation on performing and interpreting the Au simulations.

3 Vacuum arcs

Many facts, and thus, much knowledge has been accumulated about vacuum arcs in the past decades. Nevertheless, many questions regarding why exactly we observe certain behaviours remain still unanswered, or have been answered only phenomenologically. What exactly a vacuum arc is, what facts are known, and what the open questions are, is discussed with respect to this thesis below.

3.1 Definition and nature of vacuum arcs

A *vacuum arc* can be defined as an electric discharge occurring between two electrodes in vacuum. Perhaps a broader meaning is carried by the term *cathodic arcs*; these are arc discharges supplied by the cathode material which can occur either in vacuum or in the presence of an ambient gas [36]. Yet another type of arc is the *unipolar arc*; unipolar arcs are similar to vacuum arcs, only instead of striking between two solid electrodes they strike between one solid electrode and a plasma [37] (e.g. in a tokamak).

One may also distinguish between *arcs* and *sparks*. Sparks are momentary gas discharges that extinguish by themselves once the charges are neutralised; arcs are continuous discharges that are able to sustain themselves as long as energy and particles are available to the plasma. In other words, a spark consumes only the electrostatic energy that is stored in the system, while arcs are typically supplied by an external energy source as well. In another sense (which is not discussed here), sparks can also refer to chemically burning, hot particles flying off from a material, such as wood.

Unless the overall anode temperature is very high, arc discharges are always cathode-dominated [36]. That is, the plasma particles are supplied from the cathode material and the anode is only a passive electron collector. The 'footings' of the arc that supply the plasma and above which the plasma is the densest, are called *cathode spots* (Fig. 3.1). In vacuum arcs, the emission of electrons from the cathode can occur via two mechanisms: through thermionic emission, when the cathode temperature is elevated and/or through field emission, in the presence of high electric fields [31, 39].

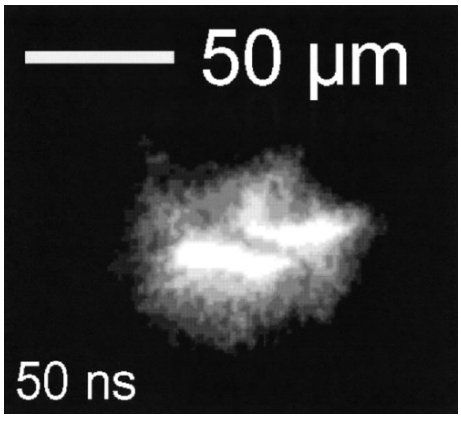

Figure 3.1: Picture of a cathode spot taken 3 µs after ignition with a high speed camera and an exposure time of 50 ns. A figure from [38].

In the context of accelerators, the term *electrical breakdown* is often used and almost always signifies vacuum arc discharges that affect the accelerator performance. How-

ever, electrical breakdowns may also occur in solid state dielectrics and in this case may not involve an arc or plasma at all.

Breakdowns in a CLIC-like environment fall into the category of vacuum arcs that are initiated due to high electric fields. The dominant electron emission mechanism is field emission. Since the electrodes are kept at room temperature, the arcs are of the cathodic type. This was also confirmed by dedicated experiments with the DC setup, which have shown that the breakdown properties depend only on the cathode material [40]. The measurement techniques of the DC setup shall be presented in Sec. 4.1.

3.2 The 'life cycle' of vacuum arcs

Below, we summarise the entire 'life cycle' of vacuum arcs that are initiated due to a high electric field. Our description is based on a phenomenological picture of vacuum arcs [20], which has become widespread in this field. A schematic illustration of the life cycle is given in Fig. 3.2.

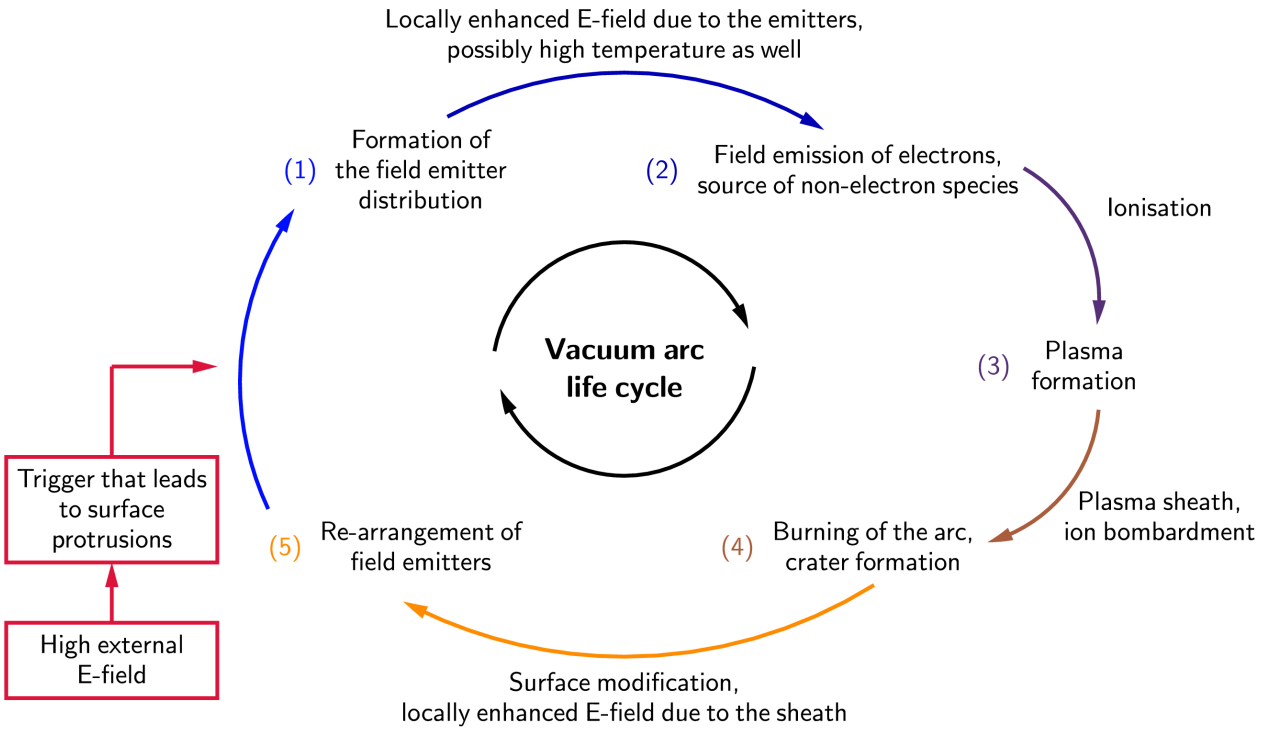

Figure 3.2: Schematic illustration of the life cycle of vacuum arcs initiated due to a high electric field in a phenomenological approach. For other types of arcs, the triggering, emission, and evaporation mechanisms may differ. Once the arc reaches stage (4), a continuous burning of the arc is initiated, while the field emitters constantly re-arrange. The life cycle ends and the vacuum arc extinguishes when the energy available to the arc is consumed.

Some surface features, like impurities or geometrical features (surface roughness, sharp edges) left over from the manufacturing and machining processes, may be present on the cathode even prior to applying any electric field. According to some theories, such features may serve as an initial field emitter that can trigger a breakdown [28]. On the other hand, assuming a well-prepared surface, the significance of such features can be negligible. Another explanation for the presence of field emitters on the cathode surface is that they form while a high external electric field is applied to the surface. From whiskers to voids [32–34], several triggering mechanisms have been proposed. However, the dominant mechanism, which might depend on the material and its preparation technique, is still not definite.

Independent of what the triggering mechanism (1) in Fig. 3.2 is, once a strong enough[1] emitter is present, the vacuum arc life cycle can be summarised as follows:

(2) The external electric field is enhanced at the emitter, and field emission of electrons occurs. The field emission current may heat the emitter significantly [33]. Due to a mixture of high electric field and temperature effects, the field emitter serves also as a source of non-electron species. As a consequence, neutrals accumulate above the emitter. At this stage, negative charges dominate above the emitter and screen the external potential. Thus the field emission current is limited by the *space charge*, that is, the spatial charge distribution, of the emitted electrons themselves.

(3) Through ionisation collisions between neutrals and electrons, more and more ions are produced. After some time, a *plasma* and with it a *plasma sheath* are formed. A plasma can be defined as a gas of particles containing a non-negligible amount of free charges, which is overall quasi-neutral and governed by a collective behaviour due to the interactions between the free charges. Whenever a plasma faces an absorbing boundary, a plasma sheath will form at that boundary, a layer in which the flow velocities of electrons and ions become balanced through a difference in densities and a corresponding sheath potential that decelerates electrons and accelerates ions.

(4) Once a plasma sheath is present, the vacuum arc enters a 'steady-state' or self-maintaining regime that is often referred to as 'burning' (which is unrelated to the word's conventional meaning of an exothermic chemical reaction). In parallel, the cathode is continuously bombarded with ions which leads to crater formation on the surface. How the vacuum arc becomes self-maintaining, and how craters can be formed during the early stage of arc burning, will be addressed in Secs. 5.2.2 and 5.4, respectively.

(5) As a consequence of ion bombardment, the cathode surface is strongly modified and the emitter distribution is re-arranged. At the same time, the electric field can be enhanced locally to high

[1] The requirements on a field emitter for a vacuum arc to form shall be discussed in Sec. 5.1.

values due to the plasma sheath, which can lead to the formation of new field emitters.

A more quantitative picture of what happens during the stages (2)–(5), and what the typical time- and length scales involved are, shall be given in this thesis. The life cycle of the vacuum arc comes to an end when the energy available to the arc is exhausted; the vacuum arc extinguishes.

3.3 Observations and facts

The plasma core near the cathode spot can have local electron number densities of up to 10^{20}–10^{22} 1/cm^3 [41, 42], nearing the density of a solid. Further away from the core, the density drops as the plasma expands into vacuum. Corresponding electron temperatures in the cathode spot are in the range 1–5 eV [43–45]. For Cu, highly ionised species up to Cu-V can be present [46], with a mean charge number of two [21].

Vacuum arcs can reach currents up to 10–100 A [21] once they are fully developed. This is also the typical range seen in experiments with the DC setup (to be discussed in detail in Sec. 5.5). Current densities in the cathode spot can be as high as 10^{11}–10^{12} A/m^2 [47, 48]. Such extreme current densities can lead to a fast destruction of sharp tips, that can serve as emitters, in less than a μs [49, 50].

At the same time, the steady-state burning voltage of an arc is rather low (usually below 100 V); for a clean Cu surface, the typical burning voltage is about 20 V [21]. The potential across the discharge gap in a fully developed arc that fills the whole discharge gap is shown schematically in Fig. 3.3. The burning voltage is defined as the voltage that drops between the anode and the cathode during the arc. Most of the burning voltage drops close to the cathode, in the plasma sheath (cathode fall). The cathode fall is material dependent and, in addition, it characterises the emission mechanism. A sheath will form at the anode as well (anode fall), which can be positive or negative depending on arc current, anode area, etc. [36].

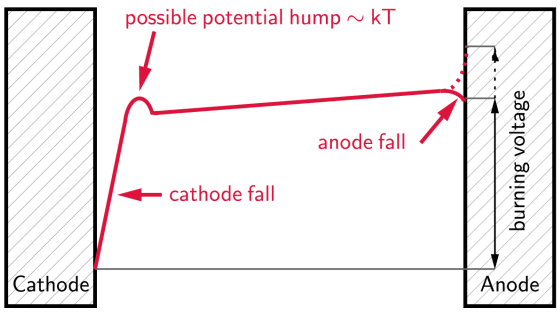

Figure 3.3: Schematic potential profile across the discharge gap. A figure adapted from [36].

The range of cathode area that is involved in the process of arcing covers many orders of magnitude. Field emission measurements carried out at 10^{-10}–10^{-9} A with the DC setup imply emission areas in the range 10^{-20}–10^{-16} m^2 [26] based on data fits to the Fowler-Nordheim equation (Eq. 3.1). In a fully developed arc, with currents up to 10–100 A, the total damaged cathode area after one arcing event is about (10–100 μm)^2 = 10^{-10}–10^{-8} m^2 [27]. Typical damage and crater shapes seen

for Cu with the DC setup and in CLIC RF cavity tests are shown in Fig. 3.4. In conclusion, both in terms of current and area, vacuum arcs can cover a range of up to 12 orders of magnitude, which is why a single modelling method can not cover the full dynamic range of the phenomenon.

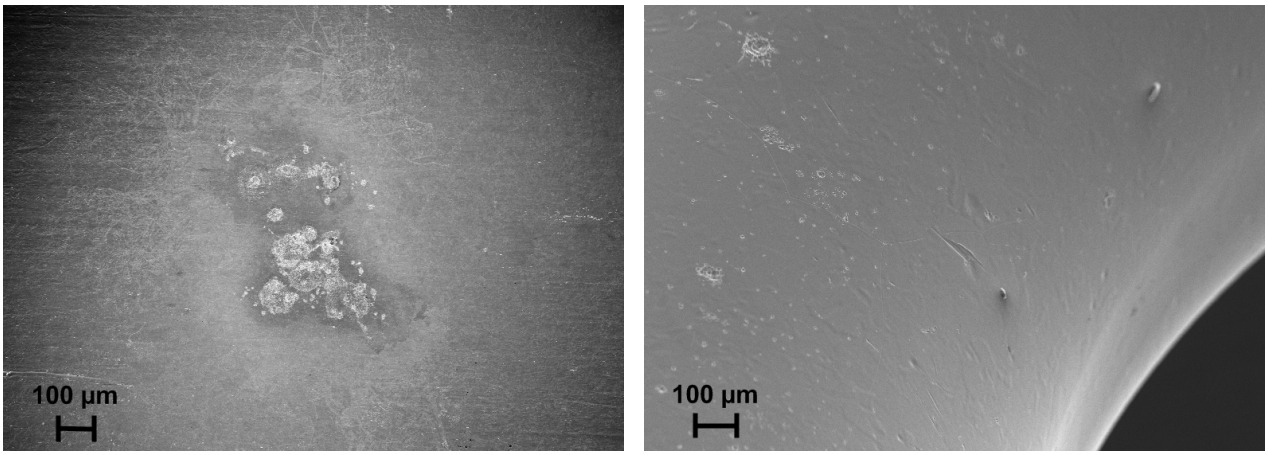

Figure 3.4: Scanning electron microscope images of the typical surface damage caused by several vacuum arcs on a Cu sample measured with the DC setup (left) and on one of the irises of the T18 CLIC test cavity (right).

3.3.1 Cathode spots and their 'movement'

Cathode spots were defined above as the footings of the arc that supply the plasma (Fig. 3.1). Cathode spots have been investigated for decades now, not only because the number and current densities can be extracted from studying them, but also because they exhibit a complex dynamic behaviour in time that can be observed through brightness fluctuations with high speed cameras.

Firstly, cathode spots have sub-structure; they seem to consist of several smaller spots. On different spatial scales, a self-similarity, or fractal-like structure of the spots was observed [51, 52], which can be related to the stochastic-deterministic nature of arc triggering [36]. Indeed, CLIC breakdown experiments also show the double nature of vacuum arc triggering: stochastic in terms of which pulse and where in the pulse the breakdown occurs [10, 53], and yet deterministic concerning the local field required for ignition (to be discussed further in Sec. 4.1).

Secondly, cathode spots seem to 'wander' around the cathode; that is, the spot itself does not move, but rather the centre of ignition changes. When a certain emission site is extinguished, another one ignites. Therefore, the plasma and with it the light emission follows the location of the strongest emitter, and thus the spot appears to 'move'. In the absence of a magnetic field, the spot 'movement' can be described with a random-walk model [54, 55]. In the presence of a magnetic field, the spot follows a retrograde motion in the $-\mathbf{j} \times \mathbf{B}$ direction [56, 57].

3.3.2 Field emission

For vacuum arcs occurring between room temperature electrodes that are exposed to a high external electric field E, the dominant electron emission mechanism is field emission. The field emission current density j_{FN} can be calculated from the electron tunneling probability over a potential barrier that is lowered by the presence of the electric field; this current density is described by the Fowler-Nordheim formulae. The original form of the Fowler-Nordheim equation was derived for the tunneling of an electron through a triangular potential barrier [58]. The form used in the experiments and simulations presented in this thesis is based on a more realistic power-law potential barrier in the Murphy and Good formulation [39, 59–61]:

$$j_{\mathrm{FN}}(E_{\mathrm{loc}}) = \frac{I_{\mathrm{FN}}(E_{\mathrm{loc}})}{A_{\mathrm{em}}} = a_{\mathrm{FN}} \frac{(eE_{\mathrm{loc}})^2}{\phi\, t(y)^2} \exp\left(-b_{\mathrm{FN}} \frac{\phi^{3/2} v(y)}{eE_{\mathrm{loc}}}\right), \tag{3.1}$$

where I_{FN} is the field emission current, A_{em} is the emission area, ϕ is the work function, e the elementary charge, and E_{loc} the local field to be defined shortly. The value $\phi = 4.5$ eV [62] has been used as an average both for polycrystalline Cu and Mo (investigated in publication **I**). $t(y)$ and $v(y)$ are elliptical integral functions of the variable

$$y = \sqrt{\frac{e^3 E_{\mathrm{loc}}}{4\pi\varepsilon_0 \phi^2}}, \tag{3.2}$$

where ε_0 is the permittivity of vacuum. The constants a_{FN} and b_{FN} stand for

$$\begin{aligned} a_{\mathrm{FN}} &= \frac{e}{16\pi^2\hbar} = 1.5414 \times 10^{-6} \frac{\mathrm{A}}{\mathrm{eV}}, \\ b_{\mathrm{FN}} &= \frac{4\sqrt{2m_{\mathrm{e}}}}{3\hbar} = 6.8309 \times 10^{9} \frac{1}{\sqrt{\mathrm{eV}}\mathrm{m}}, \end{aligned} \tag{3.3}$$

when $[j_{\mathrm{FN}}] = \mathrm{A/m^2}$, $[E_{\mathrm{loc}}] = \mathrm{V/m}$ and $[\phi] = \mathrm{eV}$, and where $\hbar$ is the reduced Planck constant and m_{e} the electron mass. The Wang and Loew approximation [63] has been used for the elliptic functions $t(y)$ and $v(y)$, setting $t(y) = 1$ and $v(y) = 0.956 - 1.062y^2$.

Unless measuring field emission very close to the surface (e.g. in field electron microscopy), the variable appearing in Eq. 3.1 is not simply E as one would expect, but is replaced with $E_{\mathrm{loc}} \stackrel{\mathrm{def.}}{=} \beta E$, containing the field enhancement factor β. This field enhancement factor is a phenomenological factor that was originally introduced as a constant, because currents obtained in field emission measurements from large areas — even though following the Fowler-Nordheim trend — turned out to be much higher than what would be expected based on purely E [61, 64].

The field enhancement factor is usually attributed to 'protrusions' on the cathode surface that can locally enhance the external electric field. One way to enhance the field is through the presence of geometrical features (emitter 'tips') that curve and densify the field lines at sharp edges. The geometrical field enhancement of a spherically rounded tip, for instance, is frequently approximated as $\beta = h/r + 2$ [65], where h is the height and r the radius of the tip. Hence, to explain the experimentally observed $\beta \lesssim 100$ for Cu, a 10 nm broad tip would have to be about 500 nm high. Nobody has ever observed such features; nevertheless, their existence cannot be excluded since they might simply not be present when the electric field is off and the surfaces are observed.

An alternative explanation of high β values is given by Schottky's conjecture on the multiplication of field enhancement factors, sometimes also called 'tip on tip' model. In this model, the final β is interpreted as a compound of a larger tip with β_l — stemming from surface roughness, for instance — and a smaller tip with β_s placed on top of it, resulting in a multiplicative enhancement of $\beta \approx \beta_l \beta_s$ [66]. Another way of obtaining an enhanced electron current could be a locally lowered work function (cf. Eq. 3.1), when impurities or crystallographic defects are present on or close to the surface.

3.4 Some open questions

It remains to be proven by future experiments which features serve as a source of enhanced field emission and how a β can be assigned to these features. What triggers an arc is also investigated in ongoing theoretical studies [34]; however, knowing the origin of β is not essential for the studies presented here. Nevertheless, it should be pointed out that β is not necessarily a constant but could depend on other quantities such as E.

All this relates to another question, namely to whether and to what extent breakdown initiation is stochastic or deterministic in its nature. RF Cu cavity tests, for instance, have shown a flat breakdown distribution over the RF pulse length [53], suggesting a purely probabilistic occurrence. In contrast, DC Cu breakdown rate experiments interleaved with field emission scans (cf. Sec. 4.1) have shown that β grows from pulse to pulse prior to breakdown and the breakdown deterministically occurs when a given E_{loc} is exceeded [67]. Future experiments are planned to investigate the stochastic/deterministic nature of breakdowns further.

Furthermore, β evolving from pulse-to-pulse indicates that the repetitive application of E could alter the surface and thus there could be a 'memory effect'. If so, β could depend on several quantities such as E, the pulse length, the energy stored in the pulse, etc. The possible dependence of β on other quantities is only one of the open questions to which experiments shall give an answer. Another essential question is how RF and DC breakdowns relate to each other and how results

obtained in one case can be translated to the other.

Once the field emission is already present, what remains to be understood is under what conditions a plasma will form and what the role of the local field in the initiation of the plasma is. Also, a plasma model should explain how this field emission can turn into a fully developed arc.

- What are the transitions the breakdown undergoes during this time?
- How do we get from nano-scale field emission areas to macroscopic damaged spots?
- Can the cathode spot expand and how can we interpret its 'movement'?
- How does the discharge gap evolve from a high-voltage open-circuit element to a low-burning-voltage plasma?

All these questions are going to be addressed in Sec. 5.

The properties of a self-maintaining arc plasma and the role of the plasma sheath in this process are yet to be determined. Furthermore, the lifetime of an arc and what makes it extinguish also need to be understood. Modelling a non-linear phenomenon, it is also desirable to investigate what factors in the numerical model may influence the results and predictions of the model.

Finally, since the interaction between the plasma and the cathode surface is essential for vacuum arcs, a link between plasma fluxes and sputtering yields should be established and incorporated into both the plasma and the surface damage model. Moreover, obtaining a better understanding of the crater formation mechanism of breakdowns could help to compare the experiments with the theory.

4 Methods

Studying vacuum arcs is a challenging task mainly because the different phenomena occurring at different stages of a vacuum arc are all interconnected and cannot be treated ignoring this connection. Therefore many areas of physics are inseparably involved in the modelling, and the choice of tools must reflect this fact. In the following, experimental as well as plasma and materials science simulation tools are presented.

4.1 Measurements with the DC setup

In the DC setup, measurements of DC vacuum arcs are carried out under UHV conditions in the pressure range 2×10^{-11}–10^{-9} mbar. Discharges are generated between a rectangular Cu sample (the cathode) and a spherically rounded Cu rod with a diameter of 2.3 mm (the anode), see Fig. 4.1. The cathode is grounded at all times and the anode is typically powered with +1–2 kV during *field emission scans* and +4–6 kV during *breakdown field measurements*. With a discharge gap separation of about 20 μm, the latter translates to an electric field of 200–300 MV/m, which is also a typical surface field in RF accelerating cavities [22, 68].

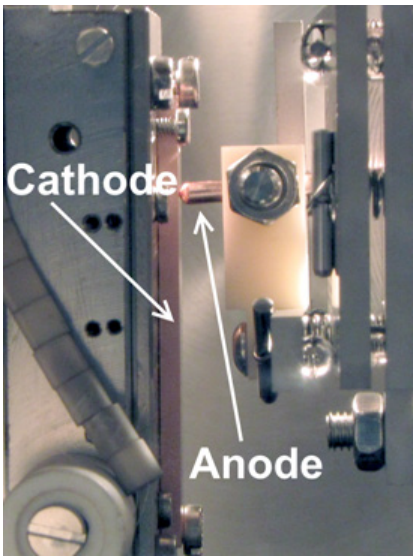

Figure 4.1: Discharge gap in one of the DC setups at CERN.

With the aid of *field emission scans*, the field emission current I_{FE} as a function of external electric field E can be obtained. Measuring in the range where space charge effects are negligible, that is 2×10^{-11}–10^{-9} A in the present setup (the lower limit corresponds to limitations in the measurement technique), the field enhancement factor β can be obtained by a fit to the Fowler-Nordheim equation (Eq. 3.1).

In *breakdown field measurements*, the external electric field is ramped up step-wise in order to determine the highest electric field that can be sustained without a breakdown occurring. This field is the breakdown field E_{b}. Note that during the voltage ramp the current rises explosively, in a very non-linear manner (cf. Eq. 3.1). Measuring E_{b} repeatedly on the same spot, some materials exhibit conditioning (e.g. Cu) and some de-conditioning (e.g. Mo), which means that after a given amount of breakdown events, E_b is higher or lower, respectively, than on an undamaged surface; i.e. processing occurs[1]. The average breakdown field that is reached *after* processing is called the

[1]Solely the cathode is processed here, since the anode is processed with breakdowns on a separate spot, before acquiring measurement data. After that, measurements are taken on another, virgin spot on the cathode.

saturated field E_{sat}; this E_{sat} characterises how 'resistant' a material is to breakdowns and thus allows us to rank materials according to this property [40, 69]. Combining field emission scans prior to breakdown and breakdown field measurements afterwards, the local field $E_{\text{loc}} = \beta E_{\text{b}}$ for Cu, after processing, was found to always have about the same value, $E_{\text{loc}}^{\text{Cu}} \sim 10$–$11$ GV/m [67].

It should be remarked that DC processing differs from RF cavity processing in mainly two aspects: (i) having different energy flows and electrostatic instead of electromagnetic fields and (ii) the area probed by the breakdown events: in DC, a small area with a radius of around 800 μm is probed over and over again, whereas in RF most of the breakdowns occur on undamaged areas.

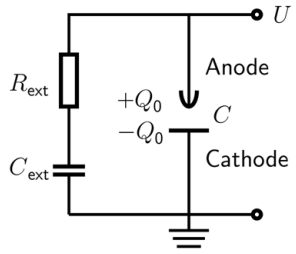

Figure 4.2: Simplified circuit diagram of the DC setup during breakdown field measurements.

In CLIC RF cavity tests, by looking at the energy balance of incident, transmitted, and reflected signals during a breakdown event, it was experimentally observed that almost all the energy stored in a pulse (about 1–10 J [70]) can be 'missing'. Currently, it cannot be directly determined how much of this missing energy is consumed by the vacuum arc itself; however, measurements with Faraday cups indicate that most of the missing energy might go into the acceleration of field emission electrons [53]. Thus the estimated typical range of energy consumption in an RF vacuum arc is about 1 mJ–1 J [68].

In the DC setup, the energy available to a vacuum arc is stored in an external capacitor; a simplified circuit is shown in Fig. 4.2. The corresponding capacitance $C_{\text{ext}} = \mathcal{O}(1\text{–}10\ \text{nF})$ is variable and allows by design the investigation of the energy range of about 1 mJ to 1 J reported in publication **I**, matching the estimated energy consumption of a breakdown in an RF cavity.

When modelling the plasma initiation on ns timescales, one should take into account that, in reality, the external capacitor is connected through a couple of metres of wire. Since the signal transmission speed is limited to the propagation speed of light, about 30 cm/ns, in the first couple of ns only the much smaller internal capacitance of the discharge gap $C \sim 1$–10 pF can serve as a source of charges.

4.2 Particle-in-cell simulations

The numerical modelling of plasmas requires methods that are quite different from e.g. methods that are used to simulate solids. The particles of interest in plasma systems are usually electrons, neutrals, and ions, and although these particles are not bound together like the particles in a lattice, they are intrinsically tied together through electromagnetic interactions. Thus, when describing plasmas, both microscopic and macroscopic information are equally important.

For the plasma simulations presented in publication **III**, the sequential 2D ARC-PIC code has been used. Plasma initiation in vacuum arcs has been simulated with total run times of up to $\sim$ 1–1.5 months, using up to 1.5 million particles. Amongst others, the 2D ARC-PIC code shall be described below.

4.2.1 Computer simulation of plasmas

In principle, the dynamics of a plasma can be fully described by the Newton-Maxwell system of equations. On the other hand, due to the usually large number of particles in a plasma and limited computational capacity, keeping track of all individual particles is in practice unrealistic; simplified approaches are necessary. Depending on whether predominantly microscopic or macroscopic information is required in the given problem and depending on applicability, a kinetic or fluid description may be used. However, the applicability of these methods is largely dependent on the collisionality of the plasma in question.

In the *fluid description*, the plasma is treated as a single macroscopic object, a 'conductive fluid', that obeys besides hydrodynamic equations also Maxwell's equations. Computational fluid models aim at determining the evolution of hydrodynamic macroscopic quantities in a system, such as mass density, current density, and macroscopic (bulk plasma) velocity. Perhaps the simplest approach is ideal magnetohydrodynamics, which is a single fluid description that treats the fluid as a perfect conductor.

More sophisticated approaches, such as multi-fluid models describing different species separately, exist as well. Generally, fluid approaches are based on assumptions concerning the equation of state, electrical resistivity, and above all, collisionality. Since fluid models are based on classical thermodynamics and hydrodynamics, the applicability of a fluid model is restricted to strongly collisional plasmas that are in quasi-static equilibrium, that is, they follow locally a Maxwell-Boltzmann distribution.

In plasmas that are far from a Maxwell-Boltzmann distribution and/or in collisionless plasmas where thermalisation cannot take place, a *kinetic description* can be used. Kinetic models aim at describing the spatial and temporal evolution of both microscopic and macroscopic quantities such as number density n, temperature T, pressure p, and local information on particle positions $\mathbf{r}$ and velocities $\mathbf{v}$ and thus can capture the velocity distribution function locally in the plasma. In a kinetic description, the macroscopic quantities need to be derived from the microscopic quantities.

Kinetic theory has its roots in assuming a weakly coupled plasma where multiple particle correlations of three or more particles can be neglected. Starting from a fundamental level, a plasma in which the number of particles for each species is conserved will obey the continuity equation of

the particle distribution function $f = f(t, \mathbf{r}, \mathbf{v})$ in phase space:

$$\frac{\mathrm{d}f}{\mathrm{d}t} = \frac{\partial f}{\partial t} + \frac{\partial (f\mathbf{v})}{\partial \mathbf{r}} + \frac{\partial (f\mathbf{a})}{\partial \mathbf{v}} = 0. \tag{4.1}$$

Here t, $\mathbf{r}$, and $\mathbf{v}$ are independent variables, so $\nabla_{\mathbf{r}} \cdot \mathbf{v} = 0$. If now the plasma is perfectly collisionless such that the particles are uncorrelated, one may assume $\nabla_{\mathbf{v}} \cdot \mathbf{a} = 0$ as well. Thus the fundamental equation of the collisionless kinetic theory, the Vlasov equation [71], takes the following form:

$$\frac{\partial f}{\partial t} + \mathbf{v} \cdot \frac{\partial f}{\partial \mathbf{r}} + \frac{\mathbf{F}}{m} \cdot \frac{\partial f}{\partial \mathbf{v}} = 0, \tag{4.2}$$

where in plasma physics applications, $\mathbf{F}$ usually stands for the Lorentz force $\mathbf{F} = q(\mathbf{E} + \mathbf{v} \times \mathbf{B})$. Collisions, however, introduce additional forces to the system and alter the evolution of the distribution f. Thus in collisional kinetic theory, by introducing a collision operator we arrive at the Boltzmann (sometimes also called the Vlasov-Fokker-Planck) equation [72]:

$$\frac{\partial f}{\partial t} + \mathbf{v} \cdot \frac{\partial f}{\partial \mathbf{r}} + \frac{\mathbf{F}}{m} \cdot \frac{\partial f}{\partial \mathbf{v}} = \left(\frac{\partial f}{\partial \mathbf{t}} \right)_{\mathrm{c}}. \tag{4.3}$$

Although the Fokker-Planck-Maxwell system has less degrees of freedom (DOF) than the original Newton-Maxwell system, fully solving Eq. 4.3 for a tokamak plasma, for instance, is currently still too demanding [73]. To reduce the complexity of the kinetic problem, gyrokinetic and gyrofluid models have been developed [74] for the simulation of magnetised plasmas. Gyrokinetic models aim at reducing one of the six DOF in Eq. 4.3 by moving to guiding-centre[2] coordinates and ignoring the rapidly changing gyrophase of the particle, while taking into account kinetic effects such as the effect of a finite Larmor radius [73]. Two main types of gyrokinetic models exist [75]: (i) the Lagrangian approach that samples the distribution function via marker particles and (ii) the Vlasov or Eulerian models that use a continuum approach to describe f.

On the boundary between kinetic and fluid description there are, for instance, gyrofluid models that construct different moments of Eq. 4.3 (or Eq. 4.2) and apply an appropriate closure, assuming thereby an equilibration of flows and currents [76]. Kinetic and fluid descriptions may also be coupled in hybrid models [77].

For the modelling of plasma initiation in vacuum arcs, the particle-in-cell method [77–80] has been applied. PIC is a commonly used method in the area of plasma physics that is based on

[2] In the presence of a uniform or spatially and/or temporally slowly varying magnetic field, the trajectory of a charged particle can be described as a superposition of a fast gyromotion around the magnetic field lines and a slow drift of the guiding centre of this gyromotion.

a kinetic description using the Lagrangian approach. The kinetic approach is essential for the modelling of the transient plasma initiation phase, where the velocity distributions are far from Maxwellian. Moreover, only the self-consistent treatment of particle-induced and external fields of the PIC method can allow for an appropriate treatment of a system where high electric fields and boundaries (absorbing walls) are present.

With the PIC method, particles are described in a continuous phase space, in a Lagrangian (moving) reference frame, while plasma macroscopic quantities (potential, densities, etc.) are discretised onto mesh points in a Eulerian (stationary) frame. Thus the two main components of a PIC code, the particle mover and the field solver, operate in different spaces. To obtain the forces acting on particles that enter the particle mover, a field interpolation method is required that interpolates the electric field from grid points to particle positions. To obtain the charge density that enters the field solver, charge assignment to the grid points has to be carried out, which extrapolates the number density from the particle positions. In order to limit the DOF in the system, the PIC method makes use of the fact that the acceleration due to the Lorentz force depends only on the charge-to-mass ratio (Eq. 4.5b) by simulating superparticles, which correspond to many real particles but are treated by the code as a single particle.

4.2.2 ARC-PIC simulation procedure and methods

Plasma initiation in vacuum arcs has been modelled with two sequential, electrostatic PIC codes: the 1D ARC-PIC code [81] and the 2D ARC-PIC code described in publications **III** and **IV**. The 1D ARC-PIC and the 2D ARC-PIC codes use a Cartesian and a cylindrically symmetric coordinate system, respectively. The discharge gap consists of two parallel electrodes in both cases. In the cylindrically symmetric system, the two coordinates are the distance from the cathode z and the distance from the symmetry axis r. Since both codes apply the same computational methods, the same simulation procedure, and differ mainly in their dimensionality, only the 2D ARC-PIC code is discussed below; the equations of the 1D ARC-PIC Cartesian code can be obtained in the limit $r = 0$.

The simulation procedure with the 2D ARC-PIC code follows the usual PIC procedure, as illustrated schematically in Fig. 4.3. The fundamental simulation time step Δt is the time step at which the fast motion of electrons is resolved. To save computation time, bigger time steps can be applied for slower processes and non-electron species. In our simulations, we used only two different time steps, setting the injection and collision time steps indicted in Fig. 4.3 to $\Delta t_{\mathrm{inj,e}} = \Delta t$ and $\Delta t_{\mathrm{inj,Cu}} = \Delta t_{\mathrm{coll,e}} = \Delta t_{\mathrm{coll,ion}} = \Delta t_{\mathrm{ion}} = 5\Delta t$.

The simulation is initialised by choosing a given set of parameters which will determine

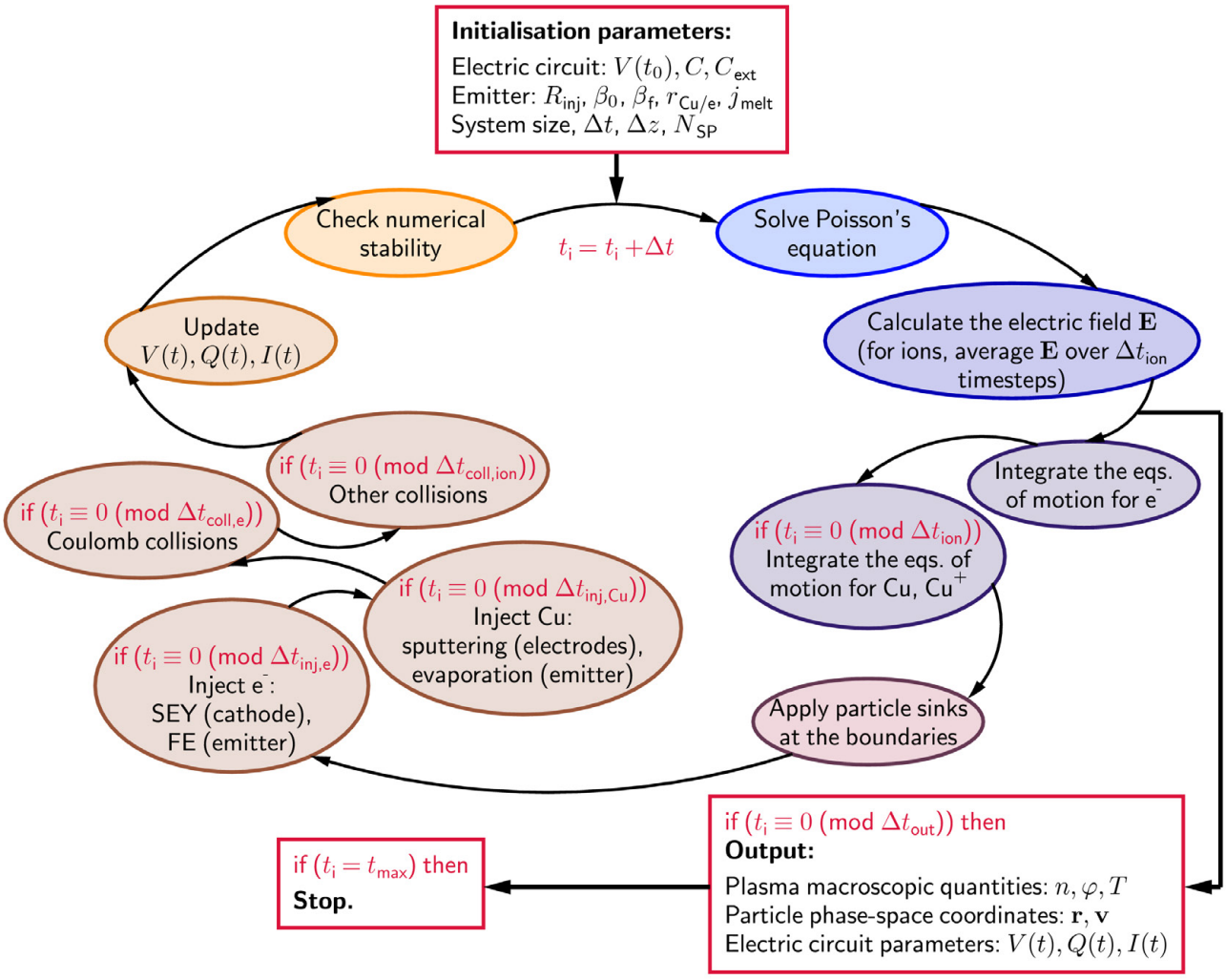

Figure 4.3: Schematic of the simulation procedure in the 2D ARC-PIC code. Some steps in the procedure are carried out only at a multiple of the fundamental time step.

- the external electric circuit,
- the properties of the field emitter,
- the system size and the numerical resolution: the time step Δt, the grid size Δz, and the real-to-superparticle ratio N_{SP}.

The numerical resolution applied in the simulation has to be suitably 'guessed' initially. To ensure the validity of this 'guess' and the stability of the solution, the fulfilment of the following stability conditions is followed regularly in the code:

$$\Delta t \lesssim 0.2\omega_{pe}^{-1}, \tag{4.4a}$$

$$\Delta z \lesssim 0.5\lambda_D, \tag{4.4b}$$

where $\omega_{\mathrm{pe}} = \sqrt{\frac{e^2 n_\mathrm{e}}{\varepsilon_0 m_\mathrm{e}}}$ is the plasma frequency and $\lambda_\mathrm{D} = \sqrt{\frac{\varepsilon_0 T_\mathrm{e}}{e^2 n_\mathrm{e}}}$ the Debye length. These constraints can be estimated considering the harmonic oscillations of a linear, unmagnetised plasma [78, 82]. The real-to-superparticle ratio has to be chosen such that the amount of particles is large enough during the field emission phase to avoid numerical instabilities and, at the same time, low enough in the final stage of the simulation to avoid memory overflow.

The simulation will start from perfect vacuum, assuming a field emitter that has the chosen characteristics. This field emitter is a source of electron field emission and Cu neutral evaporation right from the beginning. Once particles are present in the system, collisions can take place in the discharge gap and plasma-wall interactions at the boundaries. At the same time, the electric circuit parameters will determine the total energy available for breakdown, and thus the evolution of the external potential at the electrodes. The details and assumptions of the physics model incorporated into the code shall be given in Sec. 4.2.3.

Over the entire simulation time, output is generated typically a few hundred times. The output contains the phase-space coordinates of the superparticles, the macroscopic quantities of the plasma derived from these coordinates, as well as information on the particle currents at the boundaries and resulting electric circuit parameters.

Given that the simulated phenomenon can produce explosively a large amount of particles, there can be several reasons for the simulation to stop:

- the density grows so high that the stability conditions (Eq. 4.4) are not fulfilled anymore and the solution becomes unreliable,
- the number of particles grows so high that memory limitations are reached,
- the chosen total simulation time t_{max} is completed.

The 2D ARC-PIC code is a 2d3v PIC code, where particles are described in a five-dimensional phase space with two coordinates (2d) and three velocity components (3v). A uniform mesh is used with an equal grid size in both dimensions, $\Delta z = \Delta r$. The two-dimensional cylindrical system can be understood as a three-dimensional cylindrical system rotated into the same azimuthal angle, see Fig. 4.4. Thus, the volume element V increases linearly with radial distance, $V(r) \propto r$, and with it the number density n a particle corresponds to decreases as $n(r) \propto 1/r$.

The PIC particle mover solves Newton's equation using the finite difference method (FDM):

$$\Delta \mathbf{r}_\mathrm{p} = \mathbf{v}_\mathrm{p} \Delta t \,, \tag{4.5a}$$

$$\Delta \mathbf{v}_\mathrm{p} = \frac{q_\mathrm{p}}{m_\mathrm{p}} (\mathbf{E} + \mathbf{v}_\mathrm{p} \times \mathbf{B}) \Delta t \,, \tag{4.5b}$$

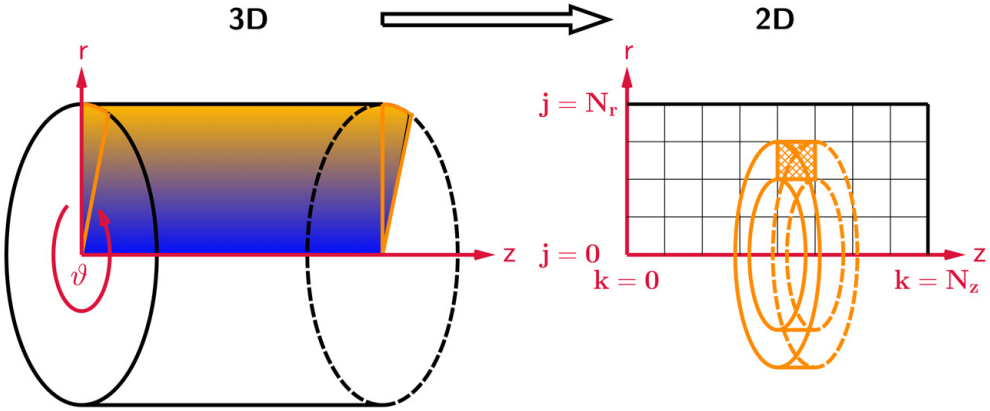

Figure 4.4: Illustration of the (r,z)-geometry of the 2D ARC-PIC code, where r is the radial coordinate and z the height coordinate (distance from the cathode).

where q_p is the charge and m_p the mass of the particle p, $\mathbf{E}$ the electric and $\mathbf{B}$ the magnetic field. The particle mover applies the Boris method [77, 83], which is an implicit solver calculating particle velocities from the already updated fields. With an optional external magnetic field the velocity updating takes the following four steps (note that velocities have three (z,r,ϑ), but fields only two components (z,r)):

$$\mathbf{v}_\mathrm{p}^\mathrm{a} = \mathbf{v}_\mathrm{p}(t_\mathrm{i}) + \frac{q_\mathrm{p}\Delta t}{2m_\mathrm{p}}\mathbf{E}, \tag{4.6a}$$

$$\mathbf{v}_\mathrm{p}^\mathrm{b} = \mathbf{v}_\mathrm{p}^\mathrm{a} + \frac{q_\mathrm{p}\Delta t}{2m_\mathrm{p}}\mathbf{v}_\mathrm{p}(t_\mathrm{i}) \times \mathbf{B}, \tag{4.6b}$$

$$\mathbf{v}_\mathrm{p}^\mathrm{c} = \mathbf{v}_\mathrm{p}^\mathrm{a} + \frac{q_\mathrm{p}\Delta t}{m_\mathrm{p}} \frac{\mathbf{v}_\mathrm{p}^\mathrm{b} \times \mathbf{B}}{1 + \left(\frac{q_\mathrm{p}\Delta t}{2m_\mathrm{p}}\right)^2 B^2}, \tag{4.6c}$$

$$\mathbf{v}_\mathrm{p}^\mathrm{d} = \mathbf{v}_\mathrm{p}^\mathrm{c} + \frac{q_\mathrm{p}\Delta t}{2m_\mathrm{p}}\mathbf{E}. \tag{4.6d}$$

Once the velocities are updated, the particles are moved:

$$z_\mathrm{p}(t_{\mathrm{i}+1}) = z_\mathrm{p}(t_\mathrm{i}) + v_{\mathrm{p},z}^\mathrm{d}\Delta t\,, \tag{4.7a}$$

$$r_\mathrm{p}(t_{\mathrm{i}+1}) = \sqrt{(r_\mathrm{p}(t_\mathrm{i}) + v_{\mathrm{p},r}^\mathrm{d}\Delta t)^2 + (v_{\mathrm{p},\vartheta}^\mathrm{d}\Delta t)^2}\,. \tag{4.7b}$$

For a non-zero ϑ-component of the velocity (originating from e.g. collisions or a magnetic field), the particles should also move in the ϑ-direction by $v_{\mathrm{p},\vartheta}\Delta t$. However, since the ϑ-coordinate is not resolved in the model, instead of moving the particles in ϑ-direction, we rotate the r- and

ϑ-components of the particle velocity into a frame where ϑ vanishes again. This rotation is determined by the angle $\alpha = \arcsin\left(\frac{v^{\mathrm{d}}_{\mathrm{p},\vartheta}\Delta t}{r_{\mathrm{p}}(t_{\mathrm{i+1}})}\right)$:

$$\begin{pmatrix} v_{\mathrm{p,r}}(t_{\mathrm{i+1}}) \\ v_{\mathrm{p},\vartheta}(t_{\mathrm{i+1}}) \end{pmatrix} = \begin{pmatrix} \cos\alpha & \sin\alpha \\ -\sin\alpha & \cos\alpha \end{pmatrix} \begin{pmatrix} v^{\mathrm{d}}_{\mathrm{p,r}} \\ v^{\mathrm{d}}_{\mathrm{p},\vartheta} \end{pmatrix}. \tag{4.8}$$

Having thus calculated the new particle positions and velocities, the updated forces and fields are obtained by solving the 2D cylindrical Poisson equation for the electric potential φ:

$$\left(\frac{\partial^2}{\partial r^2} + \frac{1}{r}\frac{1}{\partial r} + \frac{\partial^2}{\partial z^2}\right)\varphi = \frac{e}{\varepsilon_0}(n_{\mathrm{i}} - n_{\mathrm{e}}), \tag{4.9}$$

where n_{i} and n_{e} are ion and electron number densities, respectively. A five-point difference approximation is used to discretise the above expression with the FDM at a given mesh point ($z = k, r = j$):

$$\sum_{\text{5-p.}} c_{\mathrm{m}}\varphi_{\mathrm{m}} \equiv c_{\mathrm{j\text{-}1,k}}\varphi_{\mathrm{j\text{-}1,k}} + c_{\mathrm{j,k\text{-}1}}\varphi_{\mathrm{j,k\text{-}1}} + c_{\mathrm{j,k}}\varphi_{\mathrm{j,k}} + c_{\mathrm{j,k+1}}\varphi_{\mathrm{j,k+1}} + c_{\mathrm{j+1,k}}\varphi_{\mathrm{j+1,k}} = \frac{e}{\varepsilon_0}(n^{\mathrm{i}}_{\mathrm{j,k}} - n^{\mathrm{e}}_{\mathrm{j,k}}), \tag{4.10}$$

where the constants c_{m} are mesh-point dependent. The above sparse matrix inversion problem is efficiently solved with the lower-upper factorisation method using the SUPERLU package [84].

The linear cloud-in-cell scheme [77] is used to both interpolate the electric field from grid points to particle positions, and to extrapolate number densities from particle positions to grid points, see Fig. 4.5. On a uniform grid, choosing the same schemes for field interpolation and charge assignment ensures appropriate space-symmetry of forces and momentum conservation [82].

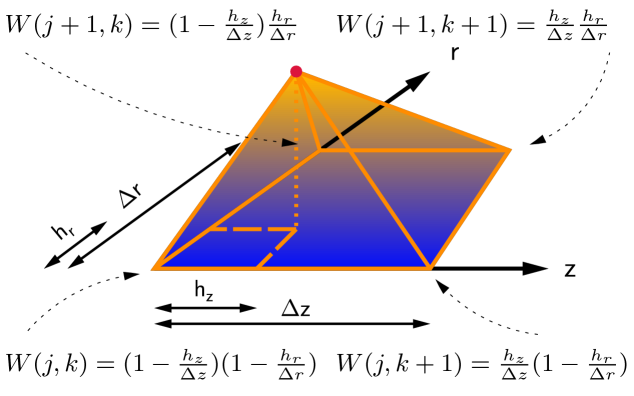

Figure 4.5: The 'shape' of a particle (red dot) in the cloud-in-cell scheme and the value of the weighting function $W = W(r,z)$ at the grid points around the particle.

Developed for the treatment of copper plasma with three species, e^-, Cu, and Cu^+, the ARC-PIC codes include collision routines developed at the Max-Planck-Institut für Plasmaphysik [85]. Collisions are described with the Monte Carlo algorithm, which is based on the

concepts developed for the direct Monte Carlo simulation of rarefied gases [86, 87]. The following interactions have been implemented, using experimentally-measured, energy-dependent cross sections:

- Coulomb collisions between the pairs (e^-, e^-), (Cu^+, Cu^+), (e^-, Cu^+) [88],
- Elastic collisions between the pairs (e^- + Cu) [89], (Cu + Cu),
- Impact ionisation: $e^- + Cu \longrightarrow 2\,e^- + Cu^+$ [90],
- Charge exchange and momentum transfer: $Cu^+ + Cu \longrightarrow Cu + Cu^+$ [91].

Elastic collisions, Cu + Cu ⟶ Cu + Cu, have been included as well. Note that, on larger length scales, Eq. 4.10 takes care of the Coulomb interactions automatically. However, as the field solver is required to be free of self-forces, inside a cell the field generated by a particle must decrease with decreasing distance from the particle. Hence, inter-particle forces inside the cells are underestimated, which is balanced with the aid of the Coulomb collisions listed above.

In all these collisions, except for the Coulomb collisions, the collision probability P_i is approximated as

$$P_\mathrm{i} = 1 - e^{-\sigma n v_\mathrm{rel} dt_\mathrm{coll}} \approx \sigma n v_\mathrm{rel} \Delta t_\mathrm{coll}\,, \tag{4.11}$$

where σ is the collision cross-section, n the local density of target particles, v_rel the relative velocity of incident particles, and Δt_coll the collision time step. Due to the long-range characteristic of the Coulomb force, the Coulomb scattering involves typically several charged particles and can be described as a diffusion process in velocity space [92]. Hence, for Coulomb collisions, a binary collision model [88] was applied. In this model, the variable $\delta = \tan\vartheta/2$, where ϑ is the scattering angle in the relative velocity frame, is chosen randomly from a Gaussian distribution such that the variance $<\delta^2>$ is given by

$$<\delta^2> = \frac{q_\alpha q_\beta n_L \ln\lambda}{8\pi\varepsilon_0^2 m_*^2 v_\mathrm{rel}^3}\Delta t_\mathrm{coll}\,, \tag{4.12}$$

where α and β denote the species, n_L is the lowest of the different species' densities, $\ln\lambda$ is the Coulomb logarithm, and m_* is the reduced mass. Impact ionisation collisions are treated with an algorithm similar to the null-collision method described in Ref. [93]. The only difference is that, in the ARC-PIC codes, the collision probability is calculated for each of the electron-neutral pairs chosen for collision, and is then compared to a random number $R \in (0, 1)$ in order to decide whether the collision takes place.

4.2.3 Physics model for the vacuum arc

Corresponding to DC experiments, a discharge gap of 20 μm is modelled with two parallel Cu electrodes. The electrodes have a 12 μm radius in the 2D model, see Fig. 4.6. The cathode is kept

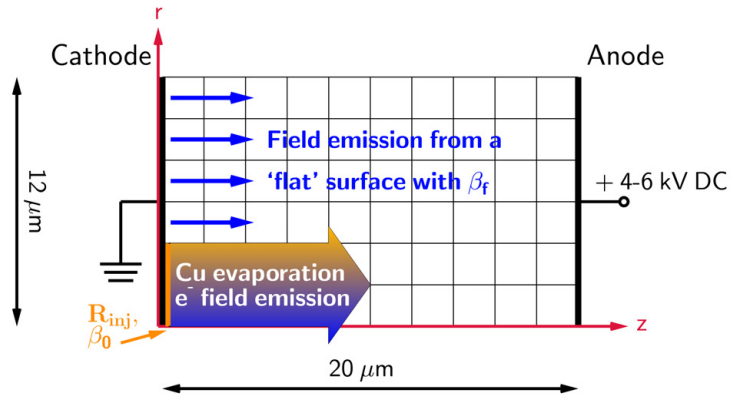

Figure 4.6: Schematic of the 2D simulation system. The 1D system corresponds to the $r = 0$ line.

at ground potential and the anode is initially powered with a voltage $V \sim +4$–6 kV, resulting in an external electric field of $E \sim 200$–300 MV/m across the gap. A uniform grid is applied to the whole simulation domain, with a grid size of typically 0.1 μm in both z and r directions. The time step is typically $\mathcal{O}(1\text{–}5$ fs) and the real-to-superparticle ratio is $\mathcal{O}(10\text{–}100)$. In the 1D model, the voltage is set to drop exponentially with a time constant τ once a current density of $2\text{–}3 \times 10^{-3}$ A/μm^2 is drawn. This value was chosen such that it corresponds to the build-up of an ion current in addition to the electron current. In the 2D model, the voltage drop is self-consistently calculated using a realistic circuit model based on Fig. 4.2, in which the energy available for breakdown is stored in capacitors. In the first 5 ns, only the capacitance of the discharge gap $C = \mathcal{O}(1\text{–}10$ pF) determines the charge Q that is available to the plasma, while later charges can also be supplied from $C_{ext} = \mathcal{O}(1\text{–}10$ nF). Knowing the charge $Q(t_i)$ and the current $I(t_i)$ at a given time step t_i, the voltage V at the next time step t_{i+1} is calculated as follows:

$$V(t_{i+1}) = \frac{Q(t_i) - I(t_i)\Delta t}{C_*}, \quad \text{where } C_* = \begin{cases} C & \text{if } (t \leq 5 \text{ ns}), \\ C_{ext} & \text{if } (t > 5 \text{ ns}), \end{cases} \tag{4.13}$$

and where $Q(t_0) = V_0 C$ and $Q(t_i = 5 \text{ ns}) = Q(t_{i-1}) + V(t_i) C_{ext} \approx V(t_i) C_{ext}$.

In the beginning, perfect vacuum and a field emitter on the cathode surface are assumed. The emitter is the source of electron field emission and Cu neutral evaporation. In the 1D simulations, only the emitter-covered part of the cathode is modelled and the area of the emitter is not resolved. In the 2D simulations, a cylindrical field emitter with an emission radius of R_{em} is modelled. In both cases, the field emitter has initially a field enhancement factor $\beta = \beta_0$, leading to a locally

enhanced field of $E_{\mathrm{loc}} = \beta_0 E$. As the emitter also evaporates, the erosion of the emitter is taken into account by linearly reducing β with the atoms evaporated; here it is assumed that the field enhancement factor represents the height to radius aspect ratio of the field emitter [29, 94]. Once a threshold electron field emission current density j_{melt} is exceeded, the 'melting' of the emitter takes place; this sets $\beta = 1$ in the 1D case and $\beta = \beta_{\mathrm{f}}$ (see below) in the 2D case. For a large enough (i.e. classically treatable) tip-like Cu protrusion $j_{\mathrm{melt}} = \mathcal{O}(10^{12}\text{–}10^{13}\ \mathrm{A/m^2})$ can be estimated based on Joule heating. Since in the 2D model R_{em} is typically $\mathcal{O}(\Delta z)$, in practice the radius of particle injection R_{inj} can be chosen to be slightly bigger than R_{em} to ensure numerical stability. In addition, in the 2D model, field emission can also occur at the 'flat' cathode surface with β_{f}. In all cases, Fowler-Nordheim emission is applied only up to $E_{\mathrm{loc}} = 12$ GV/m, which is the validity range for pure field emission [39]; above 12 GV/m, a constant extrapolation of the curve is used.

In reality, the evaporation of atoms from the emitter is due to a complex interplay of different thermal and field-related processes [32]. In lieu of a self-consistent, *ab initio* calculation of evaporation rates via MD simulations [32], a phenomenological evaporation scheme has been used in the PIC models. Motivated by the fact that the high local field can result in a high enough electron field emission current density to heat up a thin emitter significantly [33], 'field assisted thermal evaporation' is assumed that follows the field emission in a constant ratio $r_{\mathrm{Cu/e}}$. This is based on MD simulations [32, 33], which show that sharp field emitter tips, that are heated by the electron current, can lead to enhanced atom emission compared to the pure low-temperature field evaporation of ions [95].

In addition to field emission and neutral evaporation from the field emitter, different sputtering processes can take place at the electrodes and serve as further sources of electrons and neutrals:

- Cu and Cu^+ impinging at either electrode can sputter Cu with an experimentally measured, energy dependent sputtering yield [96].
- Via MD simulations, plasma ions that are accelerated over the sheath and impinge at the cathode with a high flux were shown to lead to a heat spike sputtering (see Sec. 5.4). As a result, the sputtering yield is enhanced compared to the above mentioned experimentally measured yield. Thus in PIC, above a Cu^+ flux of $6 \times 10^{23}\ 1/\mathrm{cm^2/s}$ incident to the cathode, an average sputtering yield of $Y = 1000$ is applied (cf. Fig. 5.8). Note that this enhanced sputtering yield is only applicable for high-energy ions in the early stage of arc burning, which shall be discussed in detail in Sec. 5.4.
- High-energy ions can also cause a non-negligible secondary electron yield (SEY) at the cathode. Therefore, above a Cu^+ impact energy of 100 eV, a SEY of 0.5 is applied (an estimate based on [97]).

Thus, the only source of Cu^+ ions in the model is impact ionisation collisions; all particles that are injected from the boundaries are either electrons or Cu neutrals. The injection of a given particle p is carried out in a Gaussian distribution around the velocity $v_{\mathrm{th}}^{\mathrm{p}} = \sqrt{T_{\mathrm{p}}/m_{\mathrm{p}}}$:

$$v_{\mathrm{z}}^{\mathrm{p}} = \pm\sqrt{-2\ln r_1}\, v_{\mathrm{th}}^{\mathrm{p}}, \tag{4.14a}$$

$$v_{\mathrm{r}}^{\mathrm{p}} = \sqrt{-2\ln r_2}\cos(2\pi r_3)\, v_{\mathrm{th}}^{\mathrm{p}}, \tag{4.14b}$$

$$v_{\vartheta}^{\mathrm{p}} = \sqrt{-2\ln r_2}\sin(2\pi r_3)\, v_{\mathrm{th}}^{\mathrm{p}}, \tag{4.14c}$$

where r_1, r_2, and $r_3 \in [0,1]$ are random numbers and the plus and minus sign is applied for an injection from the cathode and anode, respectively. The injection temperatures T_{p} can be adjusted.

4.3 Molecular dynamics simulations

The molecular dynamics method [98] is a suitable choice whenever one is interested in gaining microscopic information on how the phase space variables of particles (atoms or molecules) in a given system evolve; macroscopic information such as energy, temperature, and pressure can be obtained through the formalism of a thermodynamic ensemble, by calculating time averaged quantities using the ergodic hypothesis. Widely applied in materials science and chemistry, one advantage of the MD method is that it can describe crystal defects and treat collision cascades; a perfect combination for simulating the breakdown-caused surface damage on the cathode.

For the Cu surface damage simulations presented in **VI**, the fully parallel PARCAS [99] code has been used. Single crater formation events have been simulated with up to 2 000 processors, total run times of up to 200 000 h, and system sizes of up to 20 million atoms. The techniques used within PARCAS for this purpose are described below.

4.3.1 Solving the equations of motion

Given that PARCAS is based on the classical MD approach [98], it solves Newton's equation as an equation of motion for each atom p in the system:

$$\mathbf{F}_{\mathrm{p}} = m_{\mathrm{p}}\mathbf{a}_{\mathrm{p}}, \tag{4.15}$$

where $\mathbf{F}_{\mathrm{p}}$ is the force acting on the atom, m_{p} is the atom's mass and $\mathbf{a}_{\mathrm{p}}$ the resulting acceleration. Since MD treats only the atoms of a lattice, but not the electrons, information on both the interatomic forces and the close-to-equilibrium electronic effects is comprised in the potential energy V

that determines the force which an atom at position $\mathbf{r}_\mathrm{p}$ is subject to:

$$\mathbf{F}_\mathrm{p} = -(\nabla V)|_{\mathbf{r}_\mathrm{p}} \,. \tag{4.16}$$

Contrary to PIC, MD has to track small displacements in the atomic positions. The algorithm used in PARCAS for solving these equations of motion is the Gear5-algorithm [98], a fifth-order predictor-corrector algorithm, in which the solution is first 'guessed' (predicted) and then corrected to achieve the desired accuracy. Knowing the particle's position $\mathbf{r}_\mathrm{p}$, velocity $\mathbf{v}_\mathrm{p}$, and acceleration $\mathbf{a}_\mathrm{p}$ at a given time step t_i, the form of these functions at the next time step $t_{\mathrm{i}+1} = t_\mathrm{i} + \Delta t$ is first approximated with a fifth-order Taylor polynomial,

$$\mathbf{r}_\mathrm{p}^\mathrm{approx}(t_{\mathrm{i}+1}) = \mathbf{r}_\mathrm{p}(t_\mathrm{i}) + \mathbf{v}_\mathrm{p}(t_\mathrm{i})\Delta t + \frac{\mathbf{a}_\mathrm{p}(t_\mathrm{i})}{2!}\Delta t^2 + \frac{\mathbf{r}_\mathrm{p}^{(3)}(t_\mathrm{i})}{3!}\Delta t^3 + \frac{\mathbf{r}_\mathrm{p}^{(4)}(t_\mathrm{i})}{4!}\Delta t^4 + \frac{\mathbf{r}_\mathrm{p}^{(5)}(t_\mathrm{i})}{5!}\Delta t^5 \,, \tag{4.17}$$

obtaining also $\mathbf{v}_\mathrm{p}^\mathrm{approx}(t_{\mathrm{i}+1})$ and $\mathbf{a}_\mathrm{p}^\mathrm{approx}(t_{\mathrm{i}+1})$ accordingly. On the other hand, the force and the acceleration acting on the particle at the updated position $\mathbf{r}_\mathrm{p}^\mathrm{approx}(t_{\mathrm{i}+1})$ can be calculated via Eqs. 4.16 and 4.15, resulting in a more accurate, 'corrected' acceleration $\mathbf{a}_\mathrm{p}^\mathrm{corr}(t_{\mathrm{i}+1})$. Then the correction term $\Delta\mathbf{a}_\mathrm{p}(t_{\mathrm{i}+1}) = \mathbf{a}_\mathrm{p}^\mathrm{corr}(t_{\mathrm{i}+1}) - \mathbf{a}_\mathrm{p}^\mathrm{approx}(t_{\mathrm{i}+1})$ is used to calculate the corrected $\mathbf{v}_\mathrm{p}^\mathrm{corr}(t_{\mathrm{i}+1})$ and $\mathbf{r}_\mathrm{p}^\mathrm{corr}(t_{\mathrm{i}+1})$.

4.3.2 High energy effects: choice of time step and potential

The potential describing inter-atomic interactions is of central importance in MD (cf. Eq. 4.16) and must therefore by carefully chosen/constructed depending on the physics problem in question. Some important factors that need to be taken into account for the simulation of surface modification caused by the breakdown of Cu are (i) the high flux of impinging ions, to be taken into account in the time step and (ii) high-energy effects, to be taken into account in the potential.

The adaptive time step algorithm used in PARCAS [100] ensures that the time step Δt is suitably chosen for simulations of far-from-equilibrium events such as collision cascades. When energetic particles are present, Δt is decreased to guarantee sufficient accuracy (cf. Eq. 4.17) and energy conservation, and is increased for computational time saving purposes when the system is close to equilibrium. Due to the high flux of plasma ions incident on the cathode, the impact time intervals were as short as $\mathcal{O}$(1–100 fs); in comparison, a typical MD time step is $\mathcal{O}$(1 fs). Thus, special care had to be taken that there are always at least three time steps simulated between each impact event. The impact times were selected randomly from a Poisson distribution, with an average flux of about 10^{25} ions/cm^2/s (calculated with PIC simulations).

The well-tested potential by Sabochick and Lam [101–104], based on the embedded-atom method (EAM) [105, 106], was used for modelling the inter-atomic interactions in Cu. In a lattice,

long-range interactions are screened and thus in MD it is sufficient to consider only interactions between close neighbours. Therefore it is usually convenient to divide any N-body potential V into contributions coming from single particle potentials V_1, pair potentials V_2, three-body potentials V_3, etc.:

$$V = \sum_{i=1}^{N} V_1(\mathbf{r}_i) + \sum_{i=1}^{N}\sum_{j=i}^{N} V_2(\mathbf{r}_i, \mathbf{r}_j) + \sum_{i=1}^{N}\sum_{j=i}^{N}\sum_{k=j}^{N} V_3(\mathbf{r}_i, \mathbf{r}_j, \mathbf{r}_k) + \ldots, \tag{4.18}$$

where the first term V_1 is only present in case of an external field and the pair potential V_2 depends only on the distance $r_{ij} = |\mathbf{r}_i - \mathbf{r}_j|$ between the pair. In practice, the summation is carried out only over atoms that are located within a cut-off radius. Well-suited for the modelling of metals with a face-centred cubic (FCC) crystal structure, the EAM formalism uses the fact that the electron density uniquely determines the potential in a solid [107] and thus the atoms of a solid can be treated as an 'impurity' embedded in a sea of electrons. In this approach, the total energy E_{tot} of the system is expressed as a sum over atom pairs i and j of the short-range pair potential V_{ij} and the embedding energy F_i that is a functional of the electron charge density ρ_j :

$$E_{tot} = \sum_i F_i \left[\sum_{\substack{j \\ i \neq j}} \rho_j(r_{ij}) \right] + \frac{1}{2} \sum_{\substack{i,j \\ i \neq j}} V_{ij}(r_{ij}). \tag{4.19}$$

Regarding high-energy effects, techniques such as energy loss to electrons and repulsive potentials suitable for the simulation of energetic ion interactions with materials [103, 108] were used. Energy loss to electrons was added as a frictional force slowing down all atoms with a kinetic energy above that of normal thermal motions [100]. The magnitude of the force was obtained from the SRIM computer code [109]. The repulsive potential was modified to the Ziegler-Biersack-Littmark universal potential for inter-atomic separations that are clearly smaller than the equilibrium one [110].

4.3.3 Temperature control and boundary conditions

For energy to be conserved, usually a microcanonical, isolated system is modelled. However, when simulating collision cascades, the system is interacting with its surroundings; the environment serves as a heat bath of temperature T_0, absorbing the heat produced during bombardment. To avoid unphysical heating in the system, the temperature T of the system has to be adjusted.

In the bombardment simulations in publication **VI**, a temperature control method after Berendsen *et al.* [111] was utilised. With this method, a friction term is added to the equation of motion

to adjust the system temperature T to the temperature of the heat bath T_0 within a time constant $\tau = 1/(2\gamma)$:

$$\mathbf{F}_\mathrm{p} = m_\mathrm{p}\mathbf{a}_\mathrm{p} + m_\mathrm{p} v_\mathrm{p} \gamma \left(\frac{T_0}{T} - 1 \right) . \tag{4.20}$$

In practise, this is implemented by re-scaling the atom velocities by the factor

$$\lambda = \sqrt{1 + \frac{\Delta t}{\tau} \left(\frac{T_0}{T} - 1 \right)} \tag{4.21}$$

at each time step Δt.

The simulation system was assumed to be placed in an ambient temperature of $T_0 = 300$ K, to which the whole system was thermally relaxed within 1 ps prior to any bombardment. Then, in one direction, a layer of one cell was fixed at the bottom of the lattice to mimic an underlying bulk, while bombardment occurred at the top of the lattice. In the perpendicular plane, periodic boundary conditions were applied. The Berendsen temperature control was applied in a layer of five cells above the fixed layer as well as at the periodic boundaries.

5 From vacuum arc initiation to extinction

Different stages of the vacuum arc can be experimentally observed with the DC setup: field emission, breakdown, and resulting surface damage. However, the connection between these different observations remains to be established in theory. From plasma evolution to the extinction of the arc — several methods have been used to better understand the different stages and their connection. The central findings of this thesis are described below.

A crucial element in this study is the modelling of plasma initiation in vacuum arcs, because it provides a link between field emission and arc development, and thus sub-micron and macroscopic scales. Moreover, it allows for interrelating theory and measurements in several aspects. Specifically, one aim is to understand how the transition from field emission to a developed arc takes place and how the arc can maintain itself. Studying the surface damage both theoretically and experimentally is also important because here an almost direct comparison between theory and 'real life' is possible. Finally, any information, whether obtained through experiments or theory, that bridges the gap between DC and RF vacuum arcs is one step on the way to understanding the connection between the two.

5.1 Vacuum arc initiation

The starting point for the model of plasma initiation in vacuum arcs lies in the experimental evidence of typical field emission parameters measured prior to breakdown. For processed Cu, the field enhancement factor varies typically in the range $\beta \sim 30$–70, and always such that the local field leading to breakdown is around $E_{\mathrm{loc}} = 10$–11 GV/m [67]. The corresponding emission areas (cf. Eq. 3.1) covering about four orders of magnitude, $A_{\mathrm{em}} = \mathcal{O}(10^{-20}$–$10^{-16})$ m^2 [26], indicate that electron emission is initially concentrated to a nano-scale region.

The 1D and 2D plasma models are based on two assumptions. Firstly, the existence of a field emitter on the cathode surface is postulated, which is the source of electron field emission with a β typical of experiments; in the 2D model, even the emission radii (down to 100 nm) can be resolved. Secondly, a more crucial assumption is that the emitter also evaporates neutrals and that this evaporation is proportional to the field emission, with the constant of proportionality being $r_{\mathrm{Cu/e}}$. In the model, the evaporated neutrals are the first atoms that appear in the discharge gap; without these atoms, no vacuum arc would develop. Thus the time-to-breakdown is expected to have a distinct dependency on the strength of the neutral source; this dependency is discussed in Sec. 5.3.

Two requirements for plasma build-up[1] have been identified based on the 1D model in **II**. For the plasma to build up, the right combination of electrons and Cu neutrals needs to be present in the discharge gap. Firstly, field emission needs to be initially 'strong' enough in order to overcome the space charge screening of the potential. The 'strength' of the field emission can be measured in terms of j_{FN}, or alternatively, in terms of E_{loc} (cf. Eq. 3.1). Simulations with different combinations of an initial β and an external electric field E showed that, independent of the strength of the neutral source, no ionisation avalanche (see next paragraph), and thus no plasma, could be produced with $E_{\mathrm{loc}} \lesssim 8$ GV/m. However, when starting initially from $E_{\mathrm{loc}} \gtrsim 10$ GV/m, a slowly but steadily growing field emission current density was observed (as will be seen later in Fig. 5.2). This slowly but steadily growing current density is due to the first ionisations occurring in the system that start to reduce the space charge screening of the potential, and hence, lead to a rising current density.

If a strong enough neutral source is also present, this growing field emission will lead to an ionisation avalanche. Since neutrals move very slowly compared to the electrons, they accumulate over the field emitter forming a 'cloud' of neutral gas. The ionisation avalanche or 'runaway' occurs when the neutral density becomes high enough so that on average the electron mean free path of the impact ionisation, $l_{\mathrm{mfp}} = 1/(\sigma n_{\mathrm{Cu}})$, becomes smaller than the system length l_{sys}. Note that densities can vary by orders of magnitude over the system length; typically a local density of $n_{\mathrm{Cu}} \sim 10^{18}$ 1/cm^3 close to the emitter is sufficient to lead to a runaway. Once this critical neutral density is reached, plasma formation is unavoidable: ions impinging at the cathode will sputter additional neutrals, leading to a further increase in neutral density, which then again increases ionisation, sputtering, and so forth.

The identified two requirements together indicate also that the experimentally observed breakdown threshold of $E_{\mathrm{loc}} = 10$–11 GV/m might indeed be a material-dependent parameter that is determined by space-charge effects and ionisation rates in the field emission stage.

5.2 Early plasma development

The above observations reveal the necessary conditions for a vacuum arc, i.e. for a plasma to be initiated: the presence of a sufficiently strong electron and neutral source. However, they don't explain how exactly field emission turns into a developed arc when these conditions are fulfilled. During its early development, the vacuum arc goes through different stages that were studied in detail in **III**. Snapshots of these stages are shown in Fig. 5.1. Two 'transitions' can be identified: firstly, a faster transition that turns a strong field emission into a 'local arc plasma' above the field

[1] To distinguish between field emission and arc burning stages, in this thesis, the term 'plasma' is devoted to that state of matter in the discharge gap which is quasi-neutral and where a plasma sheath is present.

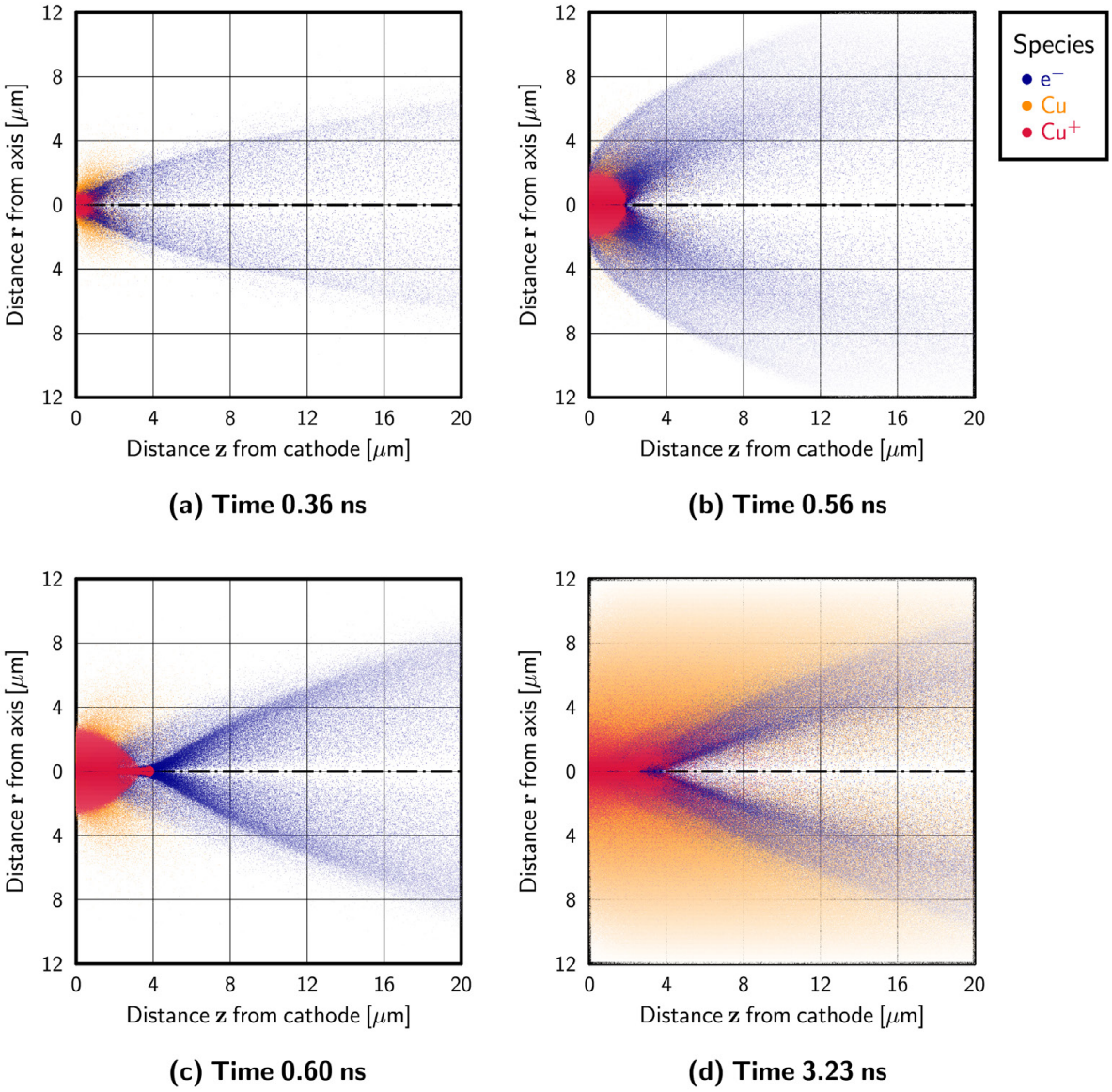

Figure 5.1: From field emission to a developed vacuum arc: different stages of the plasma initiation as simulated with the 2D ARC-PIC code. (a) early field emission, (b) field emission before the first transition, (c) local arc with a plasma sheath already being present, (d) volume-defined phase after the second transition. Only the upper half of the pictures represents the simulation domain; the lower half is a mirrored image shown to aid visualisation. Due to the cylindrical geometry of the simulation domain, the same number of particles corresponds to a lower density the greater the distance from the symmetry axis. To illustrate the r-dependency of the density, we have scaled the colour coding of the particles linearly towards white (representing vacuum) as a function of r. Corresponding number densities are shown in Fig. 5.3. A figure adapted from publication **III**.

emitter or 'cathode spot', see Fig. 5.1 (a,b) to (c); secondly, a slower transition that leads from the local arc stage to a volume-defined discharge stage, see Fig. 5.1 (c) to (d).

5.2.1 From field emission to a developed vacuum arc

In the example case of Fig. 5.1, a field emitter with an emission radius of $R_{em} = 100$ nm is assumed. An initial local field of $E_{loc} = 10.15$ GV/m is assigned to the emitter with an initial field enhancement factor $\beta_0 = 35$ and an external electric field $E = 290$ MV/m. According to Eq. 3.1, $E_{loc} = 10.15$ GV/m corresponds to a total current of $I_{FN} = 0.33$ A for the above field emitter size. However, since initially the only charged species is the system is electrons, the space-charge screening of the external potential causes the local field above the emitter to drop from the initial 10.15 GV/m to a reduced effective value E_{loc}^{SC} in the field emission stage. In the 1D simulations, this space charge effect typically reduced the local field to $E_{loc}^{SC} \approx 6$ GV/m, see Fig. 5.2 (a); however, in 1D simulations electrons can move only in one direction and thus side losses are not taken into account. In the 2D simulations, the space-charge screening will affect the local field above the emitter slightly less, due to side losses; then again, numerical fluctuations in the local field are stronger, since the particle statistics close to the axis is poorer. On average, $E_{loc}^{SC} \approx 6.4$ GV/m in the 2D case shown in Fig. 5.2 (b), corresponding to an initial space-charge corrected electron field emission current of about $I_{FN}^{SC} = \mathcal{O}(0.01\text{ A})$ in the field emission stage (discussed further in Sec. 5.3).

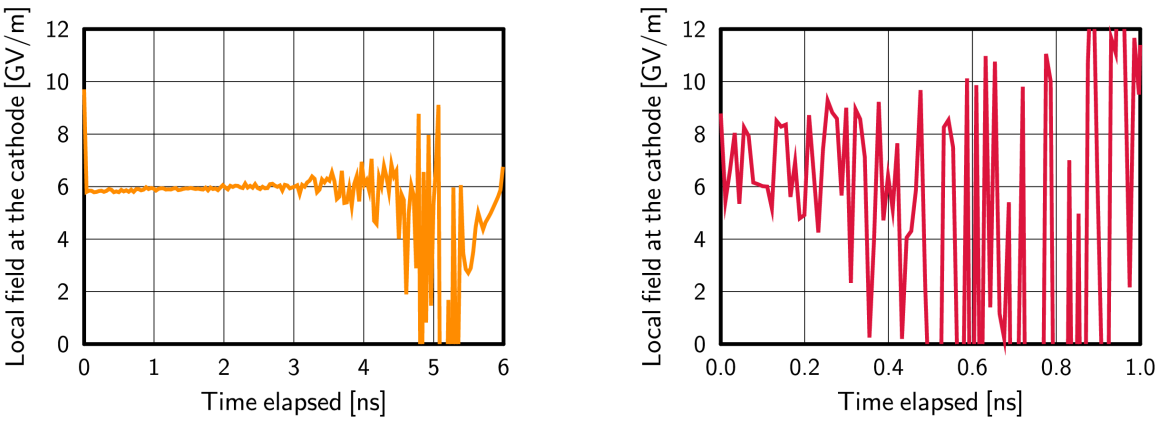

(a) 1D Arc-PIC, $\beta_0 = 40$ **(b) 2D Arc-PIC,** $\beta_0 = 35$

Figure 5.2: Evolution of local field in the field emission stage as simulated with the PIC method, which takes space-charge screening automatically into account. Fig. (b) corresponds to the case shown in Fig. 5.1. Below 0 GV/m, no field emission occurs, above 12 GV/m, the Fowler-Nordheim equation is truncated. Note that in Figs. (a) and (b) a different set of parameters was used, and in the 2D model some free parameters of the 1D model were eliminated, so the timescales cannot be compared to each other.

Then, as the first ions appear in the system, the field emission becomes slowly but steadily stronger. Just before the first transition, see Fig. 5.1 (b), the electron current increases, but electrons still spread due to space charge broadly in the radial direction. When the 'point of no return', that

is the condition for an ionisation avalanche as described in Sec. 5.1, is reached, suddenly more and more ions are produced. Since electrons move fast, a quasi-neutral plasma can be established on a sub-nanosecond timescale. As a consequence of quasi-neutrality and the presence of an absorbing boundary, a plasma sheath forms above the cathode and the ion flow towards the cathode is facilitated, resulting in a rise in total current. Also electrons exiting this local arc plasma towards the anode are now much more focussed, see Fig. 5.1 (c). Note that these focussed electrons carry most of the plasma current and thus, if the anode is close enough and the electron current density is high enough, an anode spot could develop and anode material could be evaporated.

After this first transition, neutrals slowly start to fill the discharge gap. Neutrals accumulate in the gap due to their comparatively long travel time through the gap. The timescale of this accumulation depends partly on the strength of the neutral source, which is at this stage determined by sputtering. However, the average travel time is mainly given by the injection temperature of the neutrals assumed in the model, which influences the timescale of accumulation largely. In the case of Fig. 5.1, the neutral injection temperature (cf. Eq. 4.14) was set to $T_{\mathrm{Cu}} = 14.5$ eV, and resulted in a filling time of about 4 ns. By the term 'filling time', we mean the time that is required to establish an equilibrium between neutrals entering and exiting the system. T_{Cu} was chosen such that it would match the typical temperature of sputtered atoms, which is $\mathcal{O}(10\ \mathrm{eV})$ [112], so in terms of the reference temperature $T_{\mathrm{ref}} = 2900$ eV, to which all temperatures were rescaled in our code, we picked $T_{\mathrm{Cu}} = 0.005 \times T_{\mathrm{ref}}$. The choice of $T_{\mathrm{e^-}}$ is less critical, since electrons are immediately accelerated after injection, and hence, we chose a reasonable value of $T_{\mathrm{e^-}} = 10^{-4} \times T_{\mathrm{ref}} = 0.29$ eV.

Finally, the vacuum arc enters the stage of a volume-defined discharge, see Fig. 5.1 (d), in which the plasma can fill in principle the whole discharge gap, provided that (i) there is enough time to reach this stage and (ii) the neutral density becomes high enough along the symmetry axis to lead to sufficient ionisation.

5.2.2 A self-maintaining plasma

In the region where a plasma is present, the plasma sheath, see Fig. 5.3, concentrates the external potential into a small layer above the plasma-surface interface. This leads to a local enhancement of the external electric field of up to 5–6 GV/m, see Fig. 5.4, above the original cathode spot in the case of Fig. 5.1. Since the thickness of the plasma sheath is of the order of λ_{D}, the field enhancement due to the plasma sheath is roughly given by the ratio $L_{\mathrm{pl}}/\lambda_{\mathrm{D}}$, where L_{pl} is the 'length' of the plasma.

Hence, the sheath can result in a field enhancement — at least above the original cathode spot — that is able to maintain the level of electron emission even without any other source of field enhancement. Combining this with the fact that the neutral sputtering, coming from plasma ions

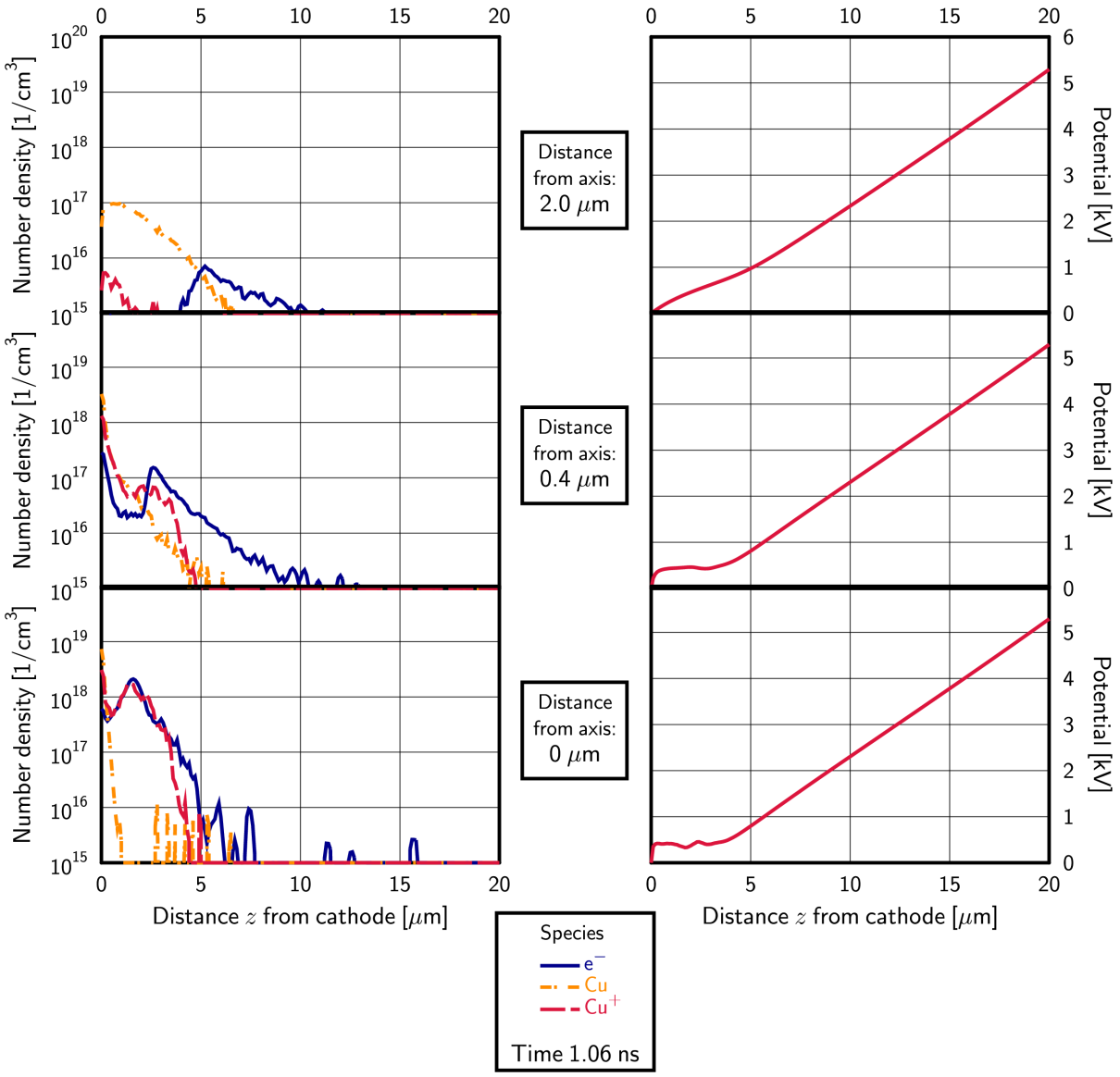

Figure 5.3: Typical number densities and potential profiles of the arc shown in Fig. 5.1 after the first transition and for three different radial distances in the system. Note that close to the axis the sheath is concentrated into a sub-micron region of $\sim$ 0.2–0.3 μm above the cathode, and that in the first $\sim$ 3–4 μm beyond the sheath the potential is flat, which is where the plasma is located, cf. Fig. 5.1. A figure adapted from publication **III**.

bombarding the cathode, leads to a volume-defined discharge phase in which the source of ions is automatically provided, it can be concluded that the plasma is self-maintaining as long as energy for the arc burning is available. Thus the presence of the plasma creates an environment that provides a sufficient flow of both electrons and neutrals from the cathode into the plasma in order to make the burning of the vacuum arc, once ignited, essentially unstoppable.

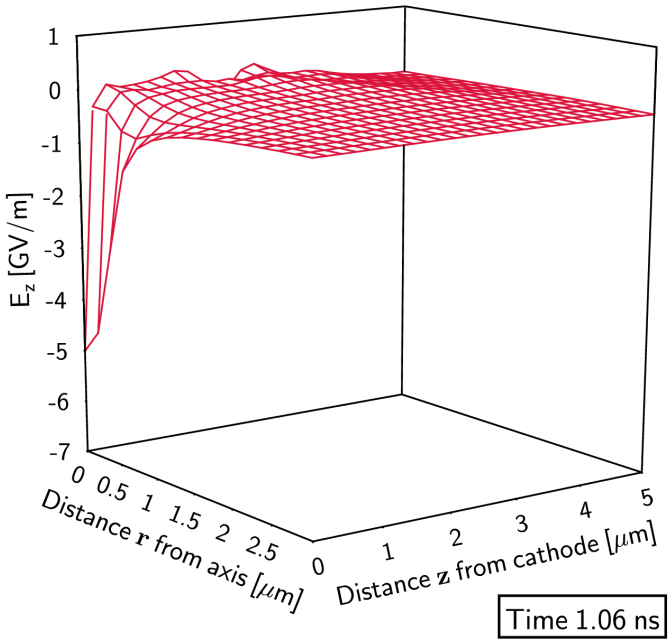

Figure 5.4: The z-component of the electric field across the discharge gap. Above the cathode spot, the electric field is locally enhanced to about 5 GV/m.

5.2.3 Plasma expansion and cathode spots

In parallel with the transitions that the vacuum arc goes through, the plasma above the cathode also expands involving a bigger and bigger surface area until the maximum current is reached (cf. Fig. 5.1). The reason for this expansion lies in the establishment of a plasma sheath, which due to its field enhancement, triggers field emission also from outside the region of the original field emitter that has an assumed average[2] $\beta_f = 2$. At the same time, neutrals spread like a gas in each direction, so ions can be created in this broader region as well; the plasma expands.

As more and more of the cathode surface serves as a source of electron emission, the footing of the plasma, that is, the cathode spot necessarily grows with the plasma. Even though simulations are limited to a few orders of magnitude in dynamic range, they demonstrate the basic mechanism of plasma and cathode spot expansion described above. This mechanism serves as a possible explanation to how field emission areas of 10^{-20}–10^{-16} m^2 [26] can turn into a vacuum arc that damages a macroscopic region of 10^{-12}–10^{-8} m^2 [27].

Thus it can be seen that even weak neighbouring field emitters — represented in the model with an average β_f — can be involved in the emission process. Hence, once the original field emitter is

[2]This choice of an average $\beta_f = 2$ was motivated by the fact that the experimentally measured field emission areas are much smaller than the resolution of our model, while, at the same time, a $\beta \lesssim 5$ was never observed in our measurements with Cu [67].

'exhausted' (that is, molten or eroded), another neighbouring field emitter can become the dominant emission site. The model suggests that, since the plasma is present over a broad cathode area, and can activate further emission sites, the plasma would re-arrange itself around this new footing. This is how the 'wandering' or 'movement' of the cathode spot can be understood within the framework of this model: not as a movement of the cathode spot itself, but as a constant re-arrangement of the plasma around the currently dominant field emitter.

5.3 Dependencies and characteristics

5.3.1 What influences the time-to-breakdown

What influence the time-to-breakdown are factors that can have an impact on how fast the first transition is reached, which is mainly depending on the the ionisation rate $\Gamma = n_{\mathrm{Cu}} n_{\mathrm{e}} \sigma v_{\mathrm{rel}}$, where σ is the cross-section of the ionisation collisions. The 'candidates' for such influencing factors are

- the strength of the neutral source determined by $r_{\mathrm{Cu/e}}$ in our model (influencing n_{Cu}),
- the details of the numerical implementation of the ionisation collisions (influencing σ),
- and factors that can affect to what speed electrons are accelerated (influencing v_{rel}).

The influence of the neutral evaporation to electron field emission ratio $r_{\mathrm{Cu/e}}$ of the field emitter with different voltage drop time constants τ has been investigated in **II**. The ratio has a very strong effect on the time-to-breakdown, see Fig. 5.5, that is, the time of the first transition to occur. This is because $r_{\mathrm{Cu/e}}$ influences the accumulation time of neutrals in the system in the field emission stage, and the first transition (the 'plasma initiation') occurs when the critical neutral density for an ionisation avalanche is reached.

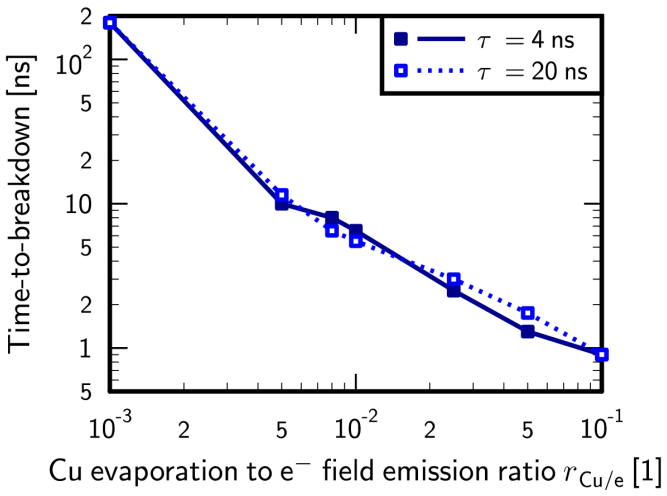

Figure 5.5: Dependence of time-to-breakdown on the neutral evaporation to electron field emission ratio for two different voltage drop time constants. A figure adapted from **II**.

The code-to-code comparison efforts described in **V** have revealed with the aid of a simplified arc model[3] that several other factors can have a substantial impact on the time-to-breakdown. One of these factors is

[3]The one-dimensional discharge model used for the code-to-code comparison assumes a constant neutral and electron flux from the cathode.

the scheme used to interpolate in-between and extrapolate outside the available data points of the energy-dependent cross-section of ionisation collisions; this scheme's influence on the time-to-breakdown is $\mathcal{O}(20\ \%)$. The specific numerical collision methods used as well as post-ionisation energy disposal can also influence the result.

Related to PIC methodology, a zeroth order (constant) scheme for the interpolation of the electric field from grid points to particle positions has proven to have insufficient accuracy (at least for the typical grid size used in the simulations). An insufficient accuracy in the field interpolation shows directly in the electron acceleration close to the cathode, since in the sheath region the electric field has strong gradients. An inaccurate estimate of the electron acceleration carries over to the relative velocity of electrons and neutrals in the impact ionisation, which in turn leads to an inaccurate estimate of ionisation rates; as a result, the time-to-breakdown can be over- or underestimated significantly ($\mathcal{O}(100\ \%)$). Moreover, an insufficient accuracy can also manifest itself in a non-convergent solution.

Due to the non-linear nature of breakdowns, the exact details of the numerical model can influence quantitative simulation results (timescales). Nevertheless, good qualitative agreement of breakdown behaviour, potential, and densities was shown with two independent codes in **V**. Bearing this in mind, quantitative results of both the 1D and the 2D plasma models should be understood as an order-of-magnitude estimate.

5.3.2 Current-voltage characteristic, burning voltage, and energy balance

From knowing the evolution of the current-voltage characteristic of vacuum arcs, essential information such as the energy consumption and the arc resistance can be extracted, information, that is also extremely valuable from an experimental point of view. With the PIC models, the early development ($\mathcal{O}(10\ \text{ns})$) of this characteristic curve has been studied (the 1D model is limited to a current-density–voltage characteristic). Two typical characteristics obtained with the 2D model are presented in Fig. 5.6.

During the field emission phase, the current I rises rather slowly and the voltage V is almost unaffected. The corresponding resistance R, if defined as $R = \mathrm{d}V/\mathrm{d}I$, is negative and rather large – the discharge gap represents an open circuit. The negative resistance is due to a rising current with dropping voltage.

As it can already be seen from Fig. 5.1, the first transition from field emission to a local vacuum arc plasma happens very fast. What limits the current from rising further than 0.4 A in this case is the amount of field emission electrons that can be supplied from the emitter. The total plasma current coming from the emitter region is mainly electron current and thus determined by the

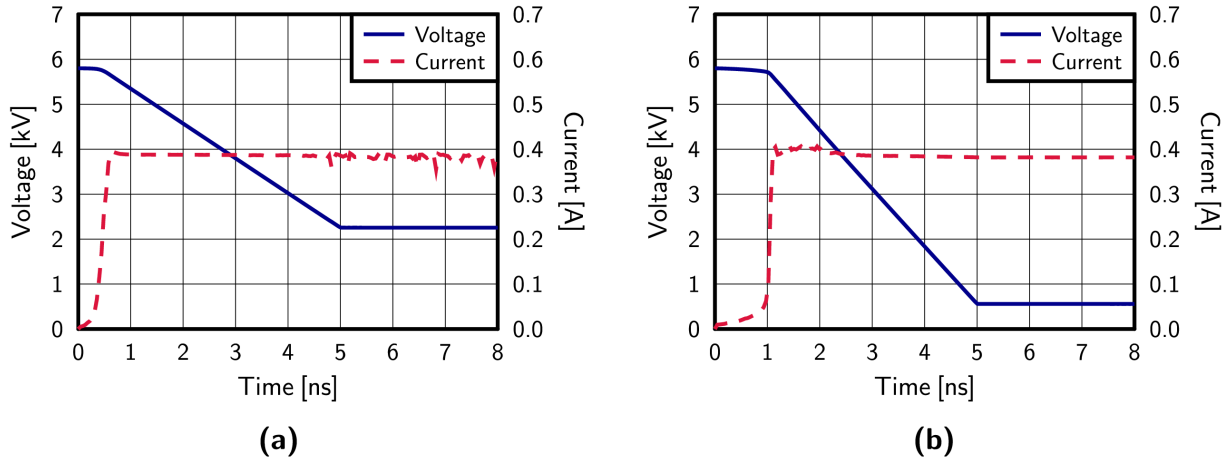

Figure 5.6: Typical current-voltage characteristics of the vacuum arc. In the first 5 ns, only the charges of the discharge gap (C) are assumed to be consumable by the arc, while after 5 ns, the charges stored in the external capacitor (C_{ext}) are also taken into account. Fig. (a) corresponds to the arc shown in Fig. 5.1 with $C = 0.5$ pF and $C_{\text{ext}} = 1$ nF, while Fig. (b) assumes $C = 0.3$ pF, $C_{\text{ext}} = 1$ nF, and a somewhat different injection scheme for evaporated neutrals. A figure adapted from **III**.

sheath's local field above the emitter resulting in a given j_{FN} and the emission area (cf. Eq. 3.1).

In reality, the emission area might grow as the current density grows (cf. Sec. 3) and several emitters could co-exist, which would lead to a further increase in total current. In the model, a constant emission area is assumed. However, due to the field enhancement of the plasma sheath, neighbouring emission sites (represented by an average β_{f}) can also be involved in the emission process. Therefore, the total current can, in some cases, grow further in the model as well as the cathode spot expands.

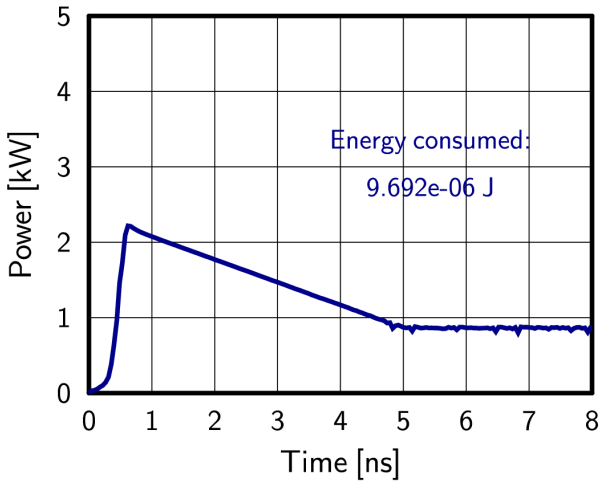

Figure 5.7: Power consumption as a function of time and integrated energy consumption corresponding to Fig. 5.6 (a). A figure adapted from **III**.

Once the plasma is established, the resistance is also reduced significantly: the presence of ions facilitates the electron current flow and a short circuit occurs. Initially, the arc can only consume the surface charges of the electrodes, and so the voltage drops

rapidly. In reality, the voltage would drop until the material-dependent burning voltage of the arc is reached (cf. Sec. 3). In the simulations, this is implicitly modelled by the charges stored in the external capacitor that are assumed to be available after 5 ns: in the limit of an infinite capacitance (where constant energy is supplied), the voltage stabilises to a constant, low value representing the burning voltage of the arc.

The power consumption as a function of time is shown in Fig. 5.7. With an initial charging voltage of 5.8 kV, the energy stored in the 0.5 pF capacitance of the discharge gap is 8.41 μJ, while the external 1 nF capacitance stores 16.82 mJ. After the first 5 ns, almost all the energy stored in the discharge gap is consumed, the voltage drops to about 2.25 kV. After that, the power consumption is kept approximately constant at around 870 W. The energy consumption calculated for the entire duration of 8 ns is 9.692 μJ, as shown in Fig. 5.7.

5.4 Early surface damage

The early-stage surface damage occurring at the cathode, due to impinging plasma ions, was studied in **VI** with the MD method. Ions were chosen to impinge on a circular area with radii in the range of $r = 3$–25 nm. The impact times of bombarding ions have been randomly chosen from a Poisson distribution using the average ion flux ($\sim 10^{25}$ ions/cm^2/s), which was calculated with PIC. The impact energies have been randomly selected from a typical ion energy distribution that the plasma has during its early stage of development, which was also determined with PIC. The average ion energy in this distribution was around 8 keV. Note that the assumption of such high energies is valid only for the initiation phase of the vacuum arc, before the burning voltage is reached, which is why the validity of the model is restricted to the early-stage surface damage.

To investigate how the degree of damage depends on the deposited dose, different doses were applied to areas always of the same size and with $r = 15$ nm. The resulting sputtering yield and crater rim size (number of adatoms) as a function of total deposited energy (dose) are shown in Fig. 5.8. A steep increase in sputtering yield occurs at around a deposited energy of 0.8 keV/nm^2, which is the energy that is needed to melt the volume

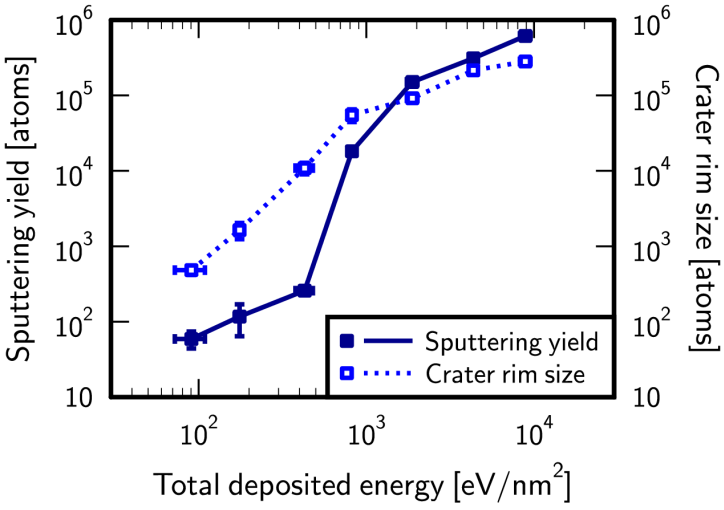

Figure 5.8: Sputtering yield and crater rim size as a function of total deposited energy (plasma ion dose). A figure adapted from **VI**.

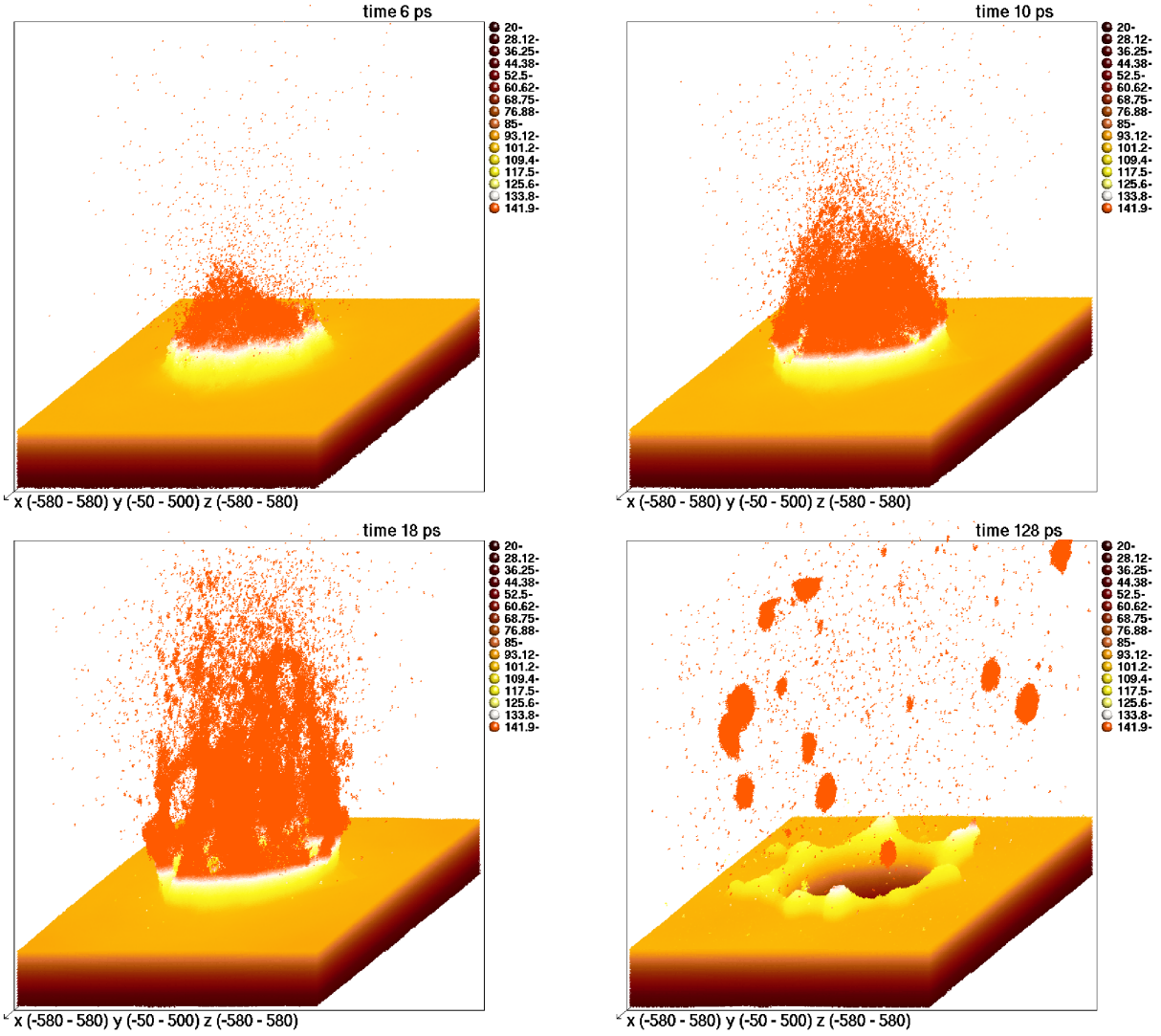

Figure 5.9: Early-stage cathode surface damage caused by energetic plasma ions. The atoms are coloured according to the height above the surface, with dark yellow corresponding to the original surface position, and light yellow and red giving the positions of atoms above the surface. The height scale is given in ångström to the right. Note the sub-nanosecond timescale that justifies the assumption of energetic ions in the early stage of a vacuum arc. A figure adapted from **VI**.

into which the energy is deposited; thus this threshold energy marks a transition.

Below the transition threshold, the crater rim size increases non-linearly with energy; however, the sputtered particles are mainly single atoms and the damage on the surface stays rather low. Since ions impinge with high energies, their penetration depth is big (up to 8 nm) and each of the ions causes a single heat spike[4] event that can heat the sample locally to very high temperatures. Below

[4]A heat spike is a many-body collision cascade in which collisions occur so densely packed that they cannot be treated independently.

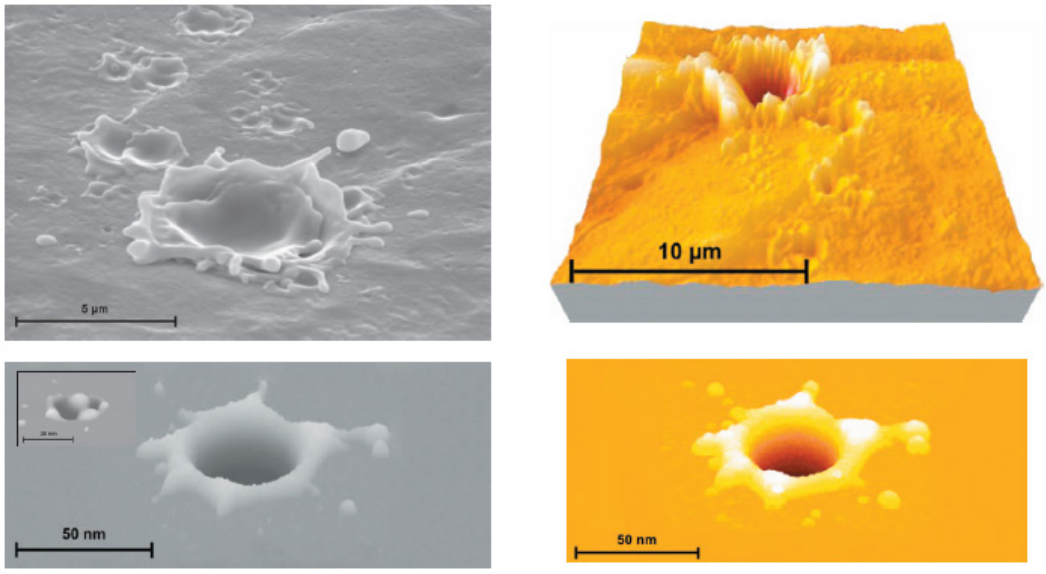

Figure 5.10: Experimentally measured and simulated crater shapes. The top row shows an SEM (left) and an AFM (right) picture of the same crater. The bottom row shows a simulated crater. A figure from **VI**.

the transition threshold, the heat spikes do not overlap yet and the craters on the surface are only created by single events; thus the sputtering yield increases roughly linearly with energy and craters remain rather shallow.

Once the threshold is reached, the dose is large enough to produce overlapping heat spikes. A large amount of material is excavated from the bulk, which is reflected in the increase in sputtering yield by more than two orders of magnitude. Craters become deeper and complex crater shapes form. Also the nature of material removal changes: sputtering occurs mainly in clusters instead of single atoms.

Above the threshold, a bigger dose will only remove material somewhat deeper from the bulk, but the mechanism of crater formation remains the same. Hence, the crater rim size and sputtering yield depend only weakly on the deposited energy above the threshold.

The sequence of events for an overlapping heat spike event is as follows, see Fig 5.9. First a hot core forms underneath the surface due to the deep penetration of ions. Once the dose is high enough, this hot core breaks the surface, material bursts out. As a consequence, complex crater shapes form that resemble experimentally observed craters. Since the material is excavated in large clusters, elongated, 'finger-like' structures can form. Part of these can remain attached to the rim of the crater, part of them breaks up into droplets that can enter the plasma or fall back onto the cathode surface to form small secondary craters.

Due to limited computational capacity (which limits the system size that can be modelled), MD-simulated craters lag 1-2 orders of magnitude behind typical experimentally observed, single side craters, see Fig. 5.10. An indication that the crater formation mechanism described above may nevertheless be valid on the larger scale of experimental craters is given by the observed self-similarity of simulated and experimental crater profiles over several orders of magnitude, see Fig 5.11.

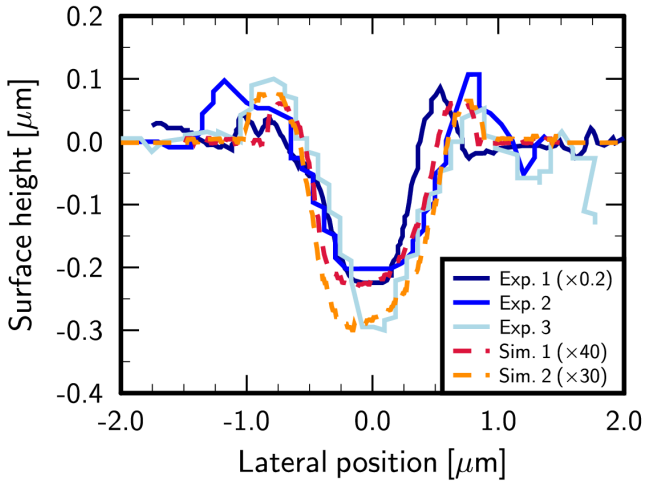

Figure 5.11: Self-similarity of experimental and simulated crater profiles. A figure adapted from **VI**.

The aspect ratio of craters, that is the ratio of the rim-to-rim width w and the average rim-to-bottom depth d of the crater, was investigated for several experimental and simulated craters. Experimentally, the crater depth was determined via atomic force microscopy (AFM), while the crater width was measured with a scanning electron microscope (SEM). The aspect ratio for experimental single-event side craters was found to be $(d/w)_{\text{exp}} = 0.26 \pm 0.04$, in good agreement with the aspect ratio of simulated craters $(d/w)_{\text{sim}} = 0.23 \pm 0.03$.

However, the above described scenario is not the only possible scenario one could think of. Crater shapes can form due to several mechanisms such as (i) high-flux single ion impact (ion 'showers'); (ii) single ion impact, if the impact energy is high enough; or (iii) cluster ion bombardment [113–116]. The relation of surface damage mechanisms due to high-flux plasma ion and cluster ion bombardment has been investigated for 500 eV Au ions in **VII**. For this study, Au was chosen because it has the same crystal structure as Cu, and well-tested inter-atomic potentials were available for the simulations [117]. Even though similar surface damage occurs in both cases, the crater formation mechanism due to cluster ions differs from the heat spike mechanism of the plasma ions described above. In the cluster ion case, fluxes are even higher, $\mathcal{O}(10^{28}–10^{29})$ atoms/cm^2/s, and the cluster impact causes a shock wave with an over-densified front followed by explosive cratering.

5.5 Extinction

Once the burning voltage of the arc is reached and stabilises, a steady-state arc burning can be achieved if the arc current is maintained with a constant, external power supply. Such a steady-state arc can then be used in industry, e.g. for arc welding. However, the breakdowns studied in this thesis are sudden, unpredictable vacuum arc discharges that extinguish as soon as the energy that

was available in the system is consumed.

CLIC RF cavities are typically operated with ∼ 250 ns long pulses (∼ 150 ns flat top) that store about 1–10 J energy [70], which gives an upper limit to the energy that can be consumed by a discharge (cf. Sec. 4.1). In case of a breakdown, due to the high arc currents, the resonant electromagnetic field in the cavity collapses on the ns timescale; the original pulse form can no longer be maintained, power is no longer transmitted. With the field collapsing, also the boundary conditions for the potential change rapidly, which makes the modelling of plasma initiation in an RF cavity harder to capture than a DC breakdown. What is, however, known from the optical spectroscopy of RF breakdowns, is that their light emission can last for 1–2 μs [53], and hence, neutrals and ions are present in the system long after the RF pulse is gone.

In the DC case, there is no pulse form. However, the boundary conditions for the potential are better-defined. Typical current-voltage characteristics measured with the DC setup are shown in Fig. 5.12.

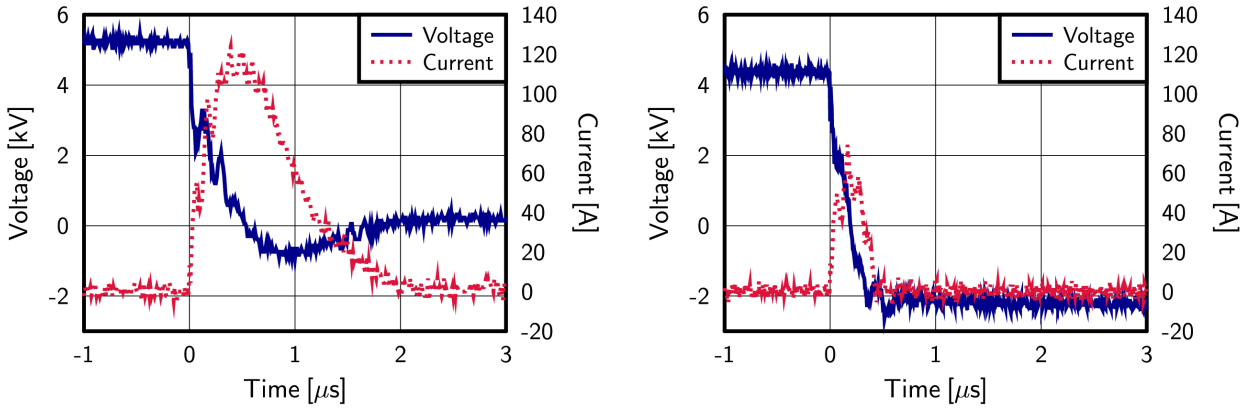

Figure 5.12: Current-voltage characteristics measured with the DC setup with different external capacitances corresponding to different energies stored in the capacitors. Note that the voltage signal cannot be reliably measured once the low-voltage regime is reached; the negative voltage is an artifact of this. Oscillations on the current and the voltage signals are due to mechanical resonances in the measurement system. A figure adapted from **I**.

The voltage drops exponentially with the time constant of the external RC-circuit. At the same time, the current rises up to its maximum. Once the energy stored in the external capacitor is used up, the voltage drops to zero. The current signal, however, can last up to a ∼ 1 μs longer, slowly decreasing to zero. This is because once the voltage is off, the charged particles of the remaining

quasi-neutral gas are externally not accelerated anymore and can survive much longer in the discharge gap. Fig. 5.12 (a) suggests a travel time of up to 1 μs and therefore an average ion velocity of 20 μm/1 μs= 20 m/s for the slowest ions. Time-resolved optical spectroscopy measurements of breakdowns generated with the DC setup confirm the presence of neutrals and ions in the system for a total of 2–3 μs [53].

In summary, it can be concluded that in both the DC and RF cases the plasma extinguishes as follows. Once the energy is consumed, the external voltage drops to zero. Electrons can no longer be supplied to the plasma. Since electrons are much faster than ions, a part of them may escape the plasma first, until an electrostatic equilibrium is reached. The remaining gas exhibits a rather long decay process of cool-down, which can be detected through the light emission of neutrals and ions, and the current signals that are seen long after the energy resources are depleted.

5.6 DC AND RF SCALING LAWS

While the investigation of DC vacuum arcs is by itself a well-defined problem with many potential applications, since our primary interest is in RF breakdowns, we would also like to understand how results obtained in the DC case translate to the RF case. Establishing scaling laws can help to resolve this problem. Despite major differences between DC and RF breakdowns, several observations indicate that the underlying physics has to be very similar in both cases.

The above mentioned optical spectroscopy results are only one example of how DC and RF cases can be compared. Earlier measurements confirmed that in the DC case the breakdown probability scales with the saturated field in the same way as breakdown rate scales with accelerating gradient in RF accelerating cavities [40]. The dependence was investigated for both Cu and Mo, and in both DC and RF cases. The underlying scaling law turns out to be universally valid for both DC and RF, but the scaling is different for Cu and Mo and is thus material dependent.

By studying then the DC energy dependence of breakdown properties in publication **I**, we have established the scaling of the saturated field with the energy available for Cu and Mo, see Fig. 5.13. Based on extensive Cu accelerating cavity testing, a similar scaling law between the accelerating gradient E_{acc} and the pulse length τ for a constant breakdown rate was derived earlier: $E_{\mathrm{acc}} \propto \tau^{-1/6}$ [9, 10]. Since the DC saturated field E_{sat} and the RF accelerating gradient E_{acc} scale in the same way with breakdown probability, and given that E_{sat} corresponds to a constant breakdown probability of about 10^{-2} [40], E_{sat} can be directly translated to E_{acc}. In addition, the RF pulse length τ can be related to the RF energy stored in a pulse $W_{\mathrm{RF}} \propto \tau V^2 \propto \tau E_{\mathrm{acc}}^2$, which can be directly compared to the energy stored in DC W_{DC}. Therefore, by replacing E_{acc} with E_{sat} and τ with W_{DC}, the RF scaling law $E_{\mathrm{acc}} \propto \tau^{-1/6}$ takes in terms of DC variables the following form:

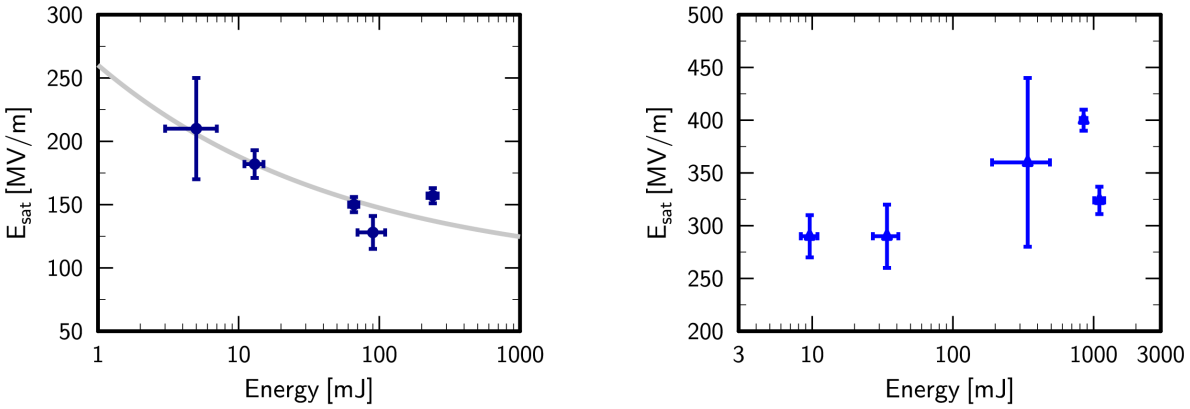

Figure 5.13: Scaling of the Cu and Mo saturated field with energy available to the discharge measured with the DC setup. Figure (a) shows in addition the corresponding RF scaling law. A figure adapted from **I**.

$E_{\mathrm{sat}} \propto W_{\mathrm{DC}}^{-1/4}$, which is shown in Fig. 5.13 (a) with a solid line. The good agreement between the DC data and the RF-based fit suggests yet another link between DC and RF.

The two main RF scaling laws for Cu, relating breakdown rate BDR, accelerating field E_{acc}, and pulse length τ as BDR$\propto E_{\mathrm{acc}}^{30}\tau^{5}$ [10], seem thus both to be valid in DC as well.

5.7 The field enhancement factor

The DC energy dependence studies presented in publication **I** indicate that the field enhancement factor of Cu scales with the energy available for breakdown as shown in Fig. 5.14.

To perform these studies, we varied the capacitor that stores the energy for breakdowns in the DC setup and measured β (via field emission scans) and E_{b} (via breakdown field measurements) alternately on the same spot. The field emission scans, that are used to determine β, were carried out with an electric circuit that is separate from the varied capacitor and are therefore unaffected by the change in capacitance. Thus, an energy dependence of β can only be explained by previous breakdowns affecting β differently depending on their energy. This could be related, for instance, to the more effective processing (cf. Sec. 4.1) of the surface observed with higher-energy breakdowns.

A scaling of β with energy would also mean that there is a 'memory effect': the surface is modified during the application of the high electric field such that the consequences of this modification remain detectable later during field emission scans. This in turn militates in favour of deterministic rather than stochastic breakdowns.

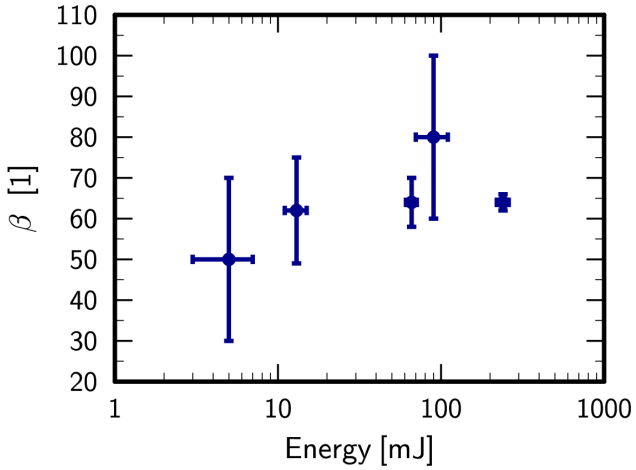

Figure 5.14: Energy dependence of the Cu field enhancement factor. A figure adapted from **I**.

In general, a dependence on the energy $W \propto E^2$ can also be translated to a dependence on the electric field E, suggesting that $\beta = \beta(W) = \beta(E)$. Indeed, since a high electric field can lead to a constant re-arrangement, growth or relaxation, of surface features (e.g. growth from voids is demonstrated in [34]), a dependence of β on E cannot be excluded. If such a dependence existed, Eq. 3.1 would have to be modified accordingly.

6 Conclusions and outlook

As a central part of this thesis, we have developed the 2D ARC-PIC code, and the physics model incorporated in it, to study plasma initiation in Cu vacuum arcs. We identified the requirements for plasma initiation as (i) a high enough initial local field of around 10 GV/m and (ii) a strong enough neutral source during the field emission phase that can produce local neutral densities of the order of 10^{18} $1/cm^3$ in the vicinity of the field emitter.

From field emission to the early stage of arc burning, we could observe two transitions. Firstly, a rapid transition from field emission to a local arc plasma that occurs due to a fast ionisation avalanche and subsequent plasma sheath formation. During this process, both the total current and the cathode area involved can grow several orders of magnitude. Secondly, a slower transition from a local arc to a volume discharge can be seen as the discharge gap is steadily filled with neutrals.

Once the arc is initiated, it is self-maintaining through a combination of (i) the plasma sheath that guarantees a sufficient electron supply from the cathode spot and (ii) intense sputtering due to ion bombardment that ensures an adequate neutral supply. The cathode spot is thus 'feeding' the arc, even if the original field emitter is not present anymore. Our simulations have explicitly shown how, due to the sheath, the cathode spot can spread sidewards, involving smaller field emitter sites into the process of arc burning. Hence, the cathode spot also has the potential to 'move' to more dominant field emitter sites once the original field emitter is exhausted. Moreover, the sidewards spreading gives a possible explanation of how the experimentally deduced field emission areas of 10^{-20}–10^{-16} m^2 [26] can lead to the experimentally observed final damaged regions of 10^{-12}–10^{-8} m^2 [27].

As a function of the neutral source strength during the field emission stage, we have given an order-of-magnitude estimate of the time-to-breakdown. However, the time-to-breakdown can be influenced by several factors in the numerical model. In this regard, our results of a code-to-code comparison carried out with two independent codes using a simplified model have shown which are the most important influencing factors and that the time-to-breakdown is reproducible, given the same conditions.

Furthermore, we have self-consistently modelled the electric circuit of the DC setup in the PIC simulations and have given thereby a qualitative prediction of the early-stage current-voltage characteristic and the energy consumption, which can help to benchmark against experiments in the future.

Coupled to PIC simulations, we have modelled the corresponding early-stage surface damage

with MD. Above a threshold deposited energy density of 0.8 keV/nm^2, the sputtering yield increases significantly. Above this threshold, sputtering occurs dominantly in clusters; finger-like structures and complex crater shapes form. Our results have shown that the crater shapes of simulated and experimentally observed DC side craters are self-similar with the same crater depth-to-width ratio of $d/w \approx 0.23$ (sim) – 0.26 (exp). Despite producing similar crater shapes, the crater formation mechanism due to high-flux single-ion bombardment was found to differ from the mechanism due to ion cluster bombardment.

We have also investigated the energy dependence of Cu and Mo breakdown properties experimentally with the DC setup. The scaling of the Cu saturated field suggests that the RF scaling law $E_{\text{acc}} \sim \tau^{-1/6}$ might also be valid for DC. Furthermore, the observed scaling of the Cu field enhancement factor with energy suggests a dynamic evolution of β with breakdowns occurring at different electric fields and energies.

Several issues remain to be explored in the future. Firstly, the starting point to the studies presented in this thesis is field emitters; how such field emitters are created, and what their field enhancement is due to, is still unknown. Secondly, the plasma model could be refined by taking into account thermal effects such as thermionic emission, the heating of the emitter, etc.; this, however, would require more information about the properties of the field emitter. Thirdly, a desirable future direction would be to achieve a better understanding of the connection between DC and RF breakdowns as well as to perform more direct benchmarking between theory and experiments, which is necessary in order to confirm fundamental assumptions in the theoretical model.

Acknowledgements

I would like to thank Prof. Juhani Keinonen, head of the Department of Physics, for giving me the opportunity to conduct research at the department and my supervisor Prof. Kai Nordlund for seeing the potential in me and guiding me throughout the years. I thoroughly enjoyed the helpful and interesting discussions I had with my project leader, Flyura Djurabekova PhD and all my colleagues in this project, Leila, Aarne, Avaz, Juha, and Stefan.

I am grateful to my CERN supervisors Sergio Calatroni dott. and Mauro Taborelli PhD for their help and the possibility to participate in the measurements. Walter Wuensch PhD, who was a mentor to me not only in the physics-related questions, deserves my special thanks for all the inspiring conversations and for always having time for me. Thanks to my colleagues and friends Anita, Christina, Rocío, Tomoko, Jan, Markus, and Nick, I had a great time at CERN, both during and outside working hours.

Above all, I would like to thank Prof. Ralf Schneider and Konstantin Matyash PhD who taught me all I know about PIC, who were always there for me, and gave me much valuable advice.

I feel deep gratitude and love for my family who always gave me strength and support.

Financial support from the EuCARD project and the Magnus Ehrnrooth foundation is gratefully acknowledged.

Geneva, 6th November 2011

Helga Timkó

Bibliography

[1] G. McCracken, *A Review of the Experimental Evidence for Arcing and Sputtering in Tokamaks*, J. Nucl. Mater. **93-94** (1980) 3.

[2] J. Hugill, *An Arc Resistant Target for the Divertor of a Fusion Reactor*, J. Nucl. Mater. **87** (1979) 353.

[3] K. Jakubka and B. Jüttner, *On the Influence of Surface Conditions on Initiation and Spot Types of Unipolar Arcs in a Tokamak*, J. Nucl. Mater. **102** (1981) 259.

[4] L. Bogomolov and A. Nedospasov, *Charge Transfer in Arcs Initiated by Disruptions in Tokamaks*, J. Nucl. Mater. **162-164** (1989) 439.

[5] M. Agarwal, M. Radhakrishnan, and A. Singh, *Application of Vacuum Arc in the Study of Unipolar Arcs in Tokamaks*, Vacuum **41** (1990) 1555.

[6] N. Rozario, H. F. Lenzing, K. F. Reardon, M. S. Zarro, and C. G. Baran, *Investigation of TELSTAR-4 spacecraft KU-band and C-band antenna components for multipactor breakdown*, IEEE T. Microw. Theory **42** (1994) 558.

[7] J. de Lara, F. Perez, M. Alfonseca, L. Galan, I. Montero, E. Roman, and D. R. Garcia-Baquero, *Multipactor prediction for on-board spacecraft RF equipment with the MEST software tool*, IEEE T. Plasma Sci. **34** (2006) 476.

[8] D. Raboso, *Multipactor breakdown: Present status and where are we heading*, 2008, At the 6th international workshop on Multipactor, Corona and Passive Intermodulation (MULCOPIM '08), Valencia, Spain.

[9] S. Doebert, C. Adolphsen, G. Bowden, D. Burke, J. Chan, V. Dolgashev, J. Frisch, K. Jobe, R. Jones, J. Lewandowski, R. Kirby, Z. Li, D. McCormick, R. Miller, C. Nantista, J. Nelson, C. Pearson, M. Ross, D. Schultz, T. Smith, S. Tantawi, J. Wang, T. Arkan, C. Boffo, H. Carter, I. Gonin, T. Khabiboulline, S. Mishra, G. Romanov, N. Solyak, Y. Funahashi, H. Hayano, N. Higashi, Y. Higashi, T. Higo, H. Kawamata, T. Kume, Y. Morozumi, K. Takata, T. Takatomi, N. Toge, K. Ueno, and Y. Watanabe, *High Gradient Performance of NLC/GLC X-Band Accelerating Structures*, in *Proceedings of the 21st Particle Accelerator Conference (PAC '05), Knoxville, USA, 2005*, pages 372 – 374, 2005.

[10] A. Grudiev, S. Calatroni, and W. Wuensch, *New local field quantity describing the high gradient limit of accelerating structures*, Phys. Rev. ST: Accel. Beams **12** (2009) 102001.

[11] S. Lee and X. Li, *Study of the Effect of Machining Parameters on the Machining Characteristics in Electrical Discharge Machining of Tungsten Carbide*, J. Mater. Process. Tech. **115** (2001) 344.

[12] A. Descoeudres, C. Hollenstein, R. Demellayer, and G. Wälder, *Optical emission spectroscopy of electrical discharge machining plasma*, J. Phys. D: Appl. Phys. **37** (2004) 875.

[13] S. K. Rao, G. M. Reddy, and K. P. Rao, *Effects of Thermo-mechanical Treatments on Mechanical Properties of AA2219 Gas Tungsten Arc Welds*, J. Mater. Process. Tech. **202** (2008) 283.

[14] A. Cevik, M. Kutuk, A. Erklig, and I. Guzelbey, *Neural Network Modeling of Arc Spot Welding*, J. Mater. Process. Tech. **202** (2008) 464.

[15] R. Bini, B. Colosimo, A. Kutlu, and M. Monno, *Experimental Study of the Features of the Kerf Generated by a 200A High Tolerance Plasma Arc Cutting System*, J. Mater. Process. Tech. **196** (2007) 345.

[16] C. D. Rakopoulos, *Evaluation of a spark-ignition engine cycle using 1st and 2nd law analysis techniques*, Energ. Convers. Manage. **34** (1993) 1299.

[17] L. S. Guo, H. B. Lu, and J. D. Li, *A hydrogen injection system with solenoid valves for a four-cylinder hydrogen-fuelled engine*, Int. J. Hydrogen Energ. **24** (1999) 377.

[18] S. Flügge, *Handbuch der Physik. Band XXII: Gasentladungen II*, 1956.

[19] L. J. Giacoletto, editor, *Electronics Designers' Handbook*, McGraw-Hill, second edition edition, 1977.

[20] R. Behrisch, *Surface Erosion by Electrical Arcs*, in *Physics of Plasma-Wall Interactions in Controlled Fusion*, edited by D. E. Post and R. Behrisch, volume 131 of *NATO ASI Series, Series B: Physics*, pages 495–513, Plenum Press, New York, 1986.

[21] B. Jüttner, *Cathode spots of electric arcs*, J. Phys. D: Appl. Phys. **34** (2001) R103.

[22] R. W. Assmann, F. Becker, R. Bossart, H. Braun, H. Burkhardt, G. Carron, W. Coosemans, R. Corsini, T. E. D'Amico, J. P. Delahaye, S. Döbert, S. D. Fartoukh, A. Ferrari, G. Geschonke, J. C. Godot, L. Groening, G. Guignard, S. Hutchins, J. B. Jeanneret, E. Jensen, J. M. Jowett, T. Kamitani, A. Millich, O. Napoly, P. Pearce, F. Perriollat, R. Pittin, J. P. Potier, T. O. Raubenheimer, A. Riche, L. Rinolfi, T. Risselada, P. Royer, F. Ruggiero, R. D. Ruth, D. Schulte, G. Suberlucq, I. V. Syratchev, L. Thorndahl, H. Trautner, A. Verdier, I. H. Wilson, W. Wuensch, F. Zhou, and F. Zimmermann, *A 3 TeV e^+e^- Linear Collider Based on CLIC Technology*, CERN, Geneva, 2000.

[23] H. Braun, R. Corsini, J. P. Delahaye, A. de Roeck, S. Döbert, A. Ferrari, G. Geschonke, A. Grudiev, C. Hauviller, B. Jeanneret, E. Jensen, T. Lefèvre, Y. Papaphilippou, G. Riddone, L. Rinolfi, W. D. Schlatter, H. Schmickler, D. Schulte, I. Syratchev, M. Taborelli, F. Tecker, R. Tomás, S. Weisz, and W. Wuensch, *CLIC 2008 Parameters*, Technical report, 2008, CLIC-Note-764.

[24] J. Wang, J. Lewandowski, J. Van Pelt, C. Yoneda, D. Gudkov, G. Riddone, T. Higo, and T. Takatomi, *Fabrication Technologies of the High Gradient Accelerator Structures at 100 MV/m Range*, in *Proceedings of the 1st International Particle Accelerator Conference (IPAC '10), Kyoto, Japan*, 2010.

[25] J.-P. Delahaye, *Towards CLIC feasibility*, in *Proceedings of the 1st International Particle Accelerator Conference (IPAC '10), Kyoto, Japan*, 2010.

[26] M. Kildemo, *New spark-test device for material characterization*, Nucl. Instrum. Meth. A **530** (2004) 596.

[27] M. Kildemo, S. Calatroni, and M. Taborelli, *Breakdown and field emission conditioning of Cu, Mo, and W*, Phys. Rev. ST: Accel. Beams **7** (2004) 092003.

[28] R. Latham, editor, *High Voltage Vacuum Insulation – Basic Concepts and Technological Practice*, Academic Press, London, 1995.

[29] G. E. Vibrans, *Field emission in vacuum voltage breakdown*, Technical report 353, Lincoln laboratory, MIT, Cambridge, Massachusetts, USA, 1964.

[30] D. W. Williams and W. T. Williams, *Field-emitted current necessary for cathode-initiated vacuum breakdown*, J. Phys. D: Appl. Phys. **5** (1972) 280.

[31] P. Rossetti, F. Paganucci, and M. Andrenucci, *Numerical model of thermoelectric phenomena leading to cathode-spot ignition*, IEEE T. Plasma Sci. **30** (2002) 1561.

[32] F. Djurabekova, S. Parviainen, A. Pohjonen, and K. Nordlund, *Atomistic modeling of metal surfaces under electric fields: Direct coupling of electric fields to a molecular dynamics algorithm*, Phys. Rev. E **83** (2011) 026704.

[33] S. Parviainen, F. Djurabekova, H. Timko, and K. Nordlund, *Electronic processes in molecular dynamics simulations of nanoscale metal tips under electric fields*, Comp. Mater. Sci. **50** (2011) 2075 .

[34] A. S. Pohjonen, F. Djurabekova, K. Nordlund, A. Kuronen, and S. P. Fitzgerald, *Dislocation nucleation from near surface void under static tensile stress in Cu*, J. Appl. Phys. **110** (2011) 023509.

[35] S. Calatroni, A. Descoeudres, J. Kovermann, M. Taborelli, H. Timko, W. Wuensch, F. Djurabekova, K. Nordlund, A. Pohjonen, and A. Kuronen, *Breakdown Studies for the CLIC Accelerating Structures*, Technical Report EuCARD-CON-2011-005, 2010.

[36] A. Anders, *Cathodic Arcs – From Fractal Spots to Energetic Condensation*, Springer Science+Business Media, LLC, 2008.

[37] J. Wesson, *Tokamaks*, Clarendon Press, Oxford, second edition, 1997, Chap. 9.8, Arcing.

[38] B. Jüttner, *Nanosecond displacement times of arc cathode spots in vacuum*, IEEE T. Plasma Sci. **27** (1999) 836.

[39] E. L. Murphy and R. H. Good, *Thermionic Emission, Field Emission, and the Transition Region*, Phys. Rev. **102** (1956) 1464.

[40] A. Descoeudres, T. Ramsvik, S. Calatroni, M. Taborelli, and W. Wuensch, *dc breakdown conditioning and breakdown rate of metals and metallic alloys under ultrahigh vacuum*, Phys. Rev. ST: Accel. Beams **12** (2009) 032001.

[41] A. Anders, S. Anders, B. Juttner, W. Botticher, H. Luck, and G. Schroder, *Pulsed dye laser diagnostics of vacuum arc cathode spots*, IEEE T. Plasma Sci. **20** (1992) 466.

[42] N. Vogel and V. Skvortsov, *Plasma parameters within the cathode spot of laser-induced vacuum arcs: experimental and theoretical investigations*, IEEE T. Plasma Sci. **25** (1997) 553.

[43] S. Anders and A. Anders, *Effects of Non-Ideality and Non-Equilibrium in the Cathode Spot Plasma of Vacuum Arcs*, Contrib. Plasm. Phys. **29** (1989) 537.

[44] E. Hantzsche, *Consequences of balance equations applied to the diffuse plasma of vacuum arcs*, IEEE T. Plasma Sci. **17** (1989) 657.

[45] N. Radic and B. Santic, *Plasma parameters within the cathode spot of the vacuum arc*, IEEE T. Plasma Sci. **17** (1989) 683.

[46] A. Anders, *Ion charge state distributions of vacuum arc plasmas: The origin of species*, Phys. Rev. E **55** (1997) 969.

[47] S. Anders, B. Jüttner, H. Pursch, and P. Siemroth, *Investigations of the Current Density in the Cathode Spot of a Vacuum Arc*, Beit. Plasmaphys. – Cont. **25** (1985) 467.

[48] P. Siemroth, T. Schulke, and T. Witke, *Microscopic high speed investigations of vacuum arc cathode spots*, IEEE T. Plasma Sci. **23** (1995) 919.

[49] W. P. Dyke and J. K. Trolan, *Field Emission: Large Current Densities, Space Charge, and the Vacuum Arc*, Phys. Rev. **89** (1953) 799.

[50] W. P. Dyke, J. K. Trolan, E. E. Martin, and J. P. Barbour, *The Field Emission Initiated Vacuum Arc. I. Experiments on Arc Initiation*, Phys. Rev. **91** (1953) 1043.

[51] T. Schülke and P. Siemroth, *Vacuum arc cathode spots as a self-similarity phenomenon*, IEEE T. Plasma Sci. **24** (1996) 63.

[52] P. Siemroth, T. Schülke, and T. Witke, *Investigation of cathode spots and plasma formation of vacuum arcs by high speed microscopy and spectroscopy*, IEEE T. Plasma Sci. **25** (1997) 571.

[53] J. W. Kovermann, *Comparative Studies of High-Gradient Rf and Dc Breakdowns*, PhD thesis, Rheinisch-Westfaelische Technische Hochschule Aachen, 2010.

[54] E. Hantzsche, B. Juttner, H. Pursch, and J. E. Daalder, *On the random walk of arc cathode spots in vacuum*, J. Phys. D: Appl. Phys. **16** (1983) L173.

[55] J. E. Daalder, *Random walk of cathode arc spots in vacuum*, J. Phys. D: Appl. Phys. **16** (1983) 17.

[56] J. Stark, *Induktionserscheinungen am Quecksilberlichtbogen im Magnetfeld*, Z. Phys. **4** (1903) 440.

[57] E. Weintraub, *Investigation of the arc in metallic vapours in an exhausted space*, Phil. Mag. **7** (1904) 95.

[58] R. H. Fowler and L. Nordheim, *Electron Emission in Intense Electric Fields*, P. Roy. Soc. Lond. A Mat. **119** (1928) 173.

[59] H. Padamsee, J. Knobloch, and T. Hays, *RF Superconductivity for Accelerators*, Wiley Series in Beam Physics and Accelerator Technology, 1998.

[60] R. G. Forbes, *Refining the application of Fowler-Nordheim theory*, Ultramicroscopy **79** (1999) 11.

[61] K. L. Jensen, Y. Y. Lau, D. W. Feldman, and P. G. O'Shea, *Electron emission contributions to dark current and its relation to microscopic field enhancement and heating in accelerator structures*, Phys. Rev. ST: Accel. Beams **11** (2008) 081001.

[62] J. Hölzl, F. Schulte, and H. Wagner, *Solid Surface Physics*, volume 85 of *Springer Tracts in Modern Physics*, Springer Berlin / Heidelberg, 1979.

[63] J. W. Wang and G. A. Loew, *Field Emission and RF Breakdown in High-Gradient Room-Temperature Linac Structures*, Technical Report SLAC-PUB-7684, Stanford Linear Accelerator Center, Stanford University, Stanford, CA 94309, USA, 1997.

[64] R. G. Forbes and K. L. Jensen, *New results in the theory of Fowler-Nordheim plots and the modelling of hemi-ellipsoidal emitters*, Ultramicroscopy **89** (2001) 17.

[65] R. G. Forbes, C. J. Edgcombe, and U. Valdrè, *Some comments on models for field enhancement*, Ultramicroscopy **95** (2003) 57.

[66] R. Miller, Y. Y. Lau, and J. H. Booske, *Schottky's conjecture on multiplication of field enhancement factors*, J. Appl. Phys. **106** (2009) 104903.

[67] A. Descoeudres, Y. Levinsen, S. Calatroni, M. Taborelli, and W. Wuensch, *Investigation of the dc vacuum breakdown mechanism*, Phys. Rev. ST: Accel. Beams **12** (2009) 092001.

[68] W. Wuensch, *High-gradient breakdown in normal-conducting RF cavities*, in *Proceedings of the 8th European Particle Accelerator Conference (EPAC '02), Paris, France*, 2002, MOYGB003.

[69] A. Descoeudres, F. Djurabekova, and K. Nordlund, *DC breakdown experiments with cobalt electrodes*, Technical report, CERN, Geneva, 2009, CLIC-Note-875.

[70] A. Grudiev and W. Wuensch, *Design of the Clic main Linac accelerating structure for Clic conceptual design report.*, Technical Report EuCARD-CON-2010-073. CERN-ATS-2010-212, CERN, Geneva, 2010.

[71] A. A. Vlasov, *The vibrational properties of an electron gas*, Soviet Physics Uspekhi **10** (1968) 721.

[72] T. J. M. Boyd and J. J. Sanderson, *The Physics of Plasmas*, Cambridge University Press, 2003.

[73] X. Garbet, Y. Idomura, L. Villard, and T. Watanabe, *Gyrokinetic simulations of turbulent transport*, Nucl. Fusion **50** (2010) 043002.

[74] R. H. Cohen and X. Q. Xu, *Progress in Kinetic Simulation of Edge Plasmas*, Contrib. Plasm. Phys. **48** (2008) 212.

[75] R. D. Sydora, *Gyrokinetic and gyrofluid theory and simulation of magnetized plasmas*, in *Computational Many-Particle Physics*, edited by Fehske, H. and Schneider, R. and Weiße, A., Springer-Verlag Berlin Heidelberg, 2008.

[76] G. L. Falchetto, B. D. Scott, P. Angelino, A. Bottino, T. Dannert, V. Grandgirard, S. Janhunen, F. Jenko, S. Jolliet, A. Kendl, B. F. McMillan, V. Naulin, A. H. Nielsen, M. Ottaviani, A. G. Peeters, M. J. Pueschel, D. Reiser, T. T. Ribeiro, and M. Romanelli, *The European turbulence code benchmarking effort: turbulence driven by thermal gradients in magnetically confined plasmas*, Plasma Phys. Contr. F. **50** (2008) 124015.

[77] C. K. Birdsall and A. B. Langdon, *Plasma Physics via Computer Simulation*, McGraw-Hill, Inc., United States of America, first edition, 1985.

[78] R. W. Hockney and J. W. Eastwood, *Computer Simulation Using Particles*, IOP Publishing Ltd, Bristol and Philadelphia, fifth edition, 1999.

[79] O. Buneman, *Dissipation of Currents in Ionized Media*, Phys. Rev. **115** (1959) 503.

[80] J. Dawson, *One-dimensional Plasma Model*, Phys. Fluids **5** (1962) 445.

[81] `1D Arc-PIC` *computer code developed at the Max-Planck Institut für Plasmaphysik, Teilinstitut Greifswald*, 2007, The main methods and algorithms used in the code are presented in Refs. [118–120].

[82] D. Tskhakaya, K. Matyash, R. Schneider, and F. Taccogna, *The Particle-In-Cell Method*, Contrib. Plasm. Phys. **47** (2007) 563.

[83] J. P. Boris, *Relativistic plasma simulation-optimization of a hybrid code*, in *Proceedings of the 4th Conference on Numerical Simulation of Plasmas*, pages 3–67, Naval Res. Lab., Washington, D.C., 1970.

[84] `SuperLU` *general purpose library*, `http://crd.lbl.gov/~xiaoye/SuperLU/`, project funded by DOE, NSF and DARPA.

[85] K. Matyash, *Kinetic modeling of multi-component edge plasmas*, PhD thesis, Ernst-Moritz-Arndt-Universität Greifswald, 2003.

[86] G. A. Bird, *Direct Simulation and the Boltzmann Equation*, Phys. Fluids **13** (1970) 2676.

[87] G. A. Bird, *Molecular gas dynamics and the direct simulation of gas flows*, Clarendon Press (Oxford and New York), 1994.

[88] T. Takizuka and H. Abe, *A binary collision model for plasma simulation with a particle code*, J. Comput. Phys. **25** (1977) 205.

[89] S. Trajmar, W. Williams, and S. K. Srivastava, *Electron-impact cross sections for Cu atoms*, J. Phys. B: At. Mol. Opt. **10** (1977) 3323.

[90] M. A. Bolorizadeh, C. J. Patton, M. B. Shah, and H. B. Gilbody, *Multiple ionization of copper by electron impact*, J. Phys. B: At. Mol. Opt. **27** (1994) 175.

[91] A. Aubreton and M.-F. Elchinger, *Transport properties in non-equilibrium argon, copper and argon–copper thermal plasmas*, J. Phys. D: Appl. Phys. **36** (2003) 1798.

[92] D. J. Larson, *A Coulomb collision model for PIC plasma simulation*, J. Comput. Phys. **188** (2003) 123.

[93] V. Vahedi and M. Surendra, *A Monte Carlo collision model for the particle-in-cell method: applications to argon and oxygen discharges*, Comput. Phys. Commun. **87** (1995) 179.

[94] P. A. Chatterton, *A theoretical study of field emission initiated vacuum breakdown*, Proc. Phys. Soc. **88** (1966) 231.

[95] R. G. Forbes, *Field evaporation theory: a review of basic ideas*, Appl. Surf. Sci. **87-88** (1995) 1, Proceedings of the 41st International Field Emission Symposium.

[96] Y. Yamamura and H. Tawara, *Energy dependence of ion-induced sputtering yields from monatomic solids at normal incidence*, Atom. Data Nucl. Data **62** (1996) 149.

[97] B. Chapman, *Glow Discharge Processes – Sputtering and Plasma Etching*, John Wiley & Sons, 1980.

[98] M. P. Allen and D. J. Tildesley, *Computer simulation of liquids*, Oxford University Press, 1989.

[99] K. Nordlund, PARCAS *computer code*, 2011, The main methods and algorithms used in the code are presented in Refs. [102] and [103].

[100] K. Nordlund, *Molecular dynamics simulation of ion ranges in the 1-100 keV energy range*, Comp. Mater. Sci. **3** (1995) 448.

[101] M. J. Sabochick and N. Q. Lam, *Radiation-Induced Amorphization of Ordered Intermetallic Compounds CuTi, $CuTi_3$, and Cu_4Ti_3 A molecular-dynamics study*, Phys. Rev. B **43** (1991) 5243.

[102] K. Nordlund, M. Ghaly, R. S. Averback, M. Caturla, T. Diaz de la Rubia, and J. Tarus, *Defect production in collision cascades in elemental semiconductors and fcc metals*, Phys. Rev. B **57** (1998) 7556.

[103] M. Ghaly, K. Nordlund, and R. Averback, *Molecular Dynamics Investigations of Surface Damage Produced by keV Self-Bombardment of Solids*, Philos. Mag. A **79** (1999) 795.

[104] K. Nordlund, J. Keinonen, M. Ghaly, and R. S. Averback, *Coherent displacement of atoms during ion irradiation*, Nature (London) **398** (1999) 49.

[105] M. Daw and M. Baskes, *Semiempirical, Quantum Mechanical Calculation of Hydrogen Embrittlement in Metals*, Phys. Rev. Lett. **50** (1983) 1285.

[106] M. Daw and M. Baskes, *Embedded-atom Method: Derivation and Application to Impurities, Surfaces and other Defects in Metals*, Phys. Rev. B **29** (1984) 6443.

[107] P. Hohenberg and W. Kohn, *Inhomogeneous Electron Gas*, Phys. Rev. **136** (1964) B864.

[108] J. Samela and K. Nordlund, *Atomistic Simulation of the Transition from Atomistic to Macroscopic Cratering*, Phys. Rev. Lett. **101** (2008) 027601.

[109] J. F. Ziegler, SRIM-2003 software package, available online at http://www.srim.org.

[110] J. F. Ziegler, J. P. Biersack, and U. Littmark, *The Stopping and Range of Ions in Matter*, Pergamon, New York, 1985.

[111] H. J. C. Berendsen, J. P. M. Postma, W. F. van Gunsteren, A. DiNola, and J. R. Haak, *Molecular dynamics with coupling to an external bath*, J. Chem. Phys. **81** (1984) 3684.

[112] W. O. Hofer, *Sputtering by Particle Bombardment III*, chapter 2. Angular, Energy and Mass Distribution of Sputtered Particles, Springer, Berlin, 1991.

[113] H. M. Urbassek and K. T. Waldeer, *Spikes in condensed rare gases induced by keV-atom bombardment*, Phys. Rev. Lett. **67** (1991) 105.

[114] M. Ghaly and R. S. Averback, *Effect of viscous flow on ion damage near solid surfaces*, Phys. Rev. Lett. **72** (1994) 364.

[115] T. J. Colla, R. Aderjan, R. Kissel, and H. M. Urbassek, *Sputtering of Au (111) induced by 16-keV Au cluster bombardment: Spikes, craters, late emission, and fluctuations*, Phys. Rev. B **62** (2000) 8487.

[116] K. Nordlund, T. Järvi, K. Meinander, and J. Samela, *Cluster ion-solid interactions from meV to MeV energies*, Appl. Phys. A: Mater. **91** (2008) 561.

[117] J. Samela, J. Kotakoski, K. Nordlund, and J. Keinonen, *A quantitative and comparative study of sputtering yields in Au*, Nucl. Instr. Meth. Phys. Res. B **239** (2005) 331.

[118] K. Matyash, R. Schneider, F. Taccogna, A. Hatayama, S. Longo, M. Capitelli, D. Tskhakaya, and F. X. Bronold, *Particle in Cell Simulation of Low Temperature Laboratory Plasmas*, Contrib. Plasm. Phys. **47** (2007) 595.

[119] K. Matyash, R. Schneider, K. Dittmann, J. Meichsner, F. X. Bronold, and D. Tskhakaya, *Radio-frequency discharges in oxygen: III. Comparison of modelling and experiment*, J. Phys. D: Appl. Phys. **40** (2007) 6601.

[120] F. X. Bronold, K. Matyash, D. Tskhakaya, R. Schneider, and H. Fehske, *Radio-frequency discharges in oxygen: I. Particle-based modelling*, J. Phys. D: Appl. Phys. **40** (2007) 6583.